THE UNIVERSITY OF TEXAS AT AUSTIN

AN EXPERIMENTAL INVESTIGATION OF SUPERSONIC FLOW PAST A WEDGE-CYLINDER CONFIGURATION

Daniel W. Barnette

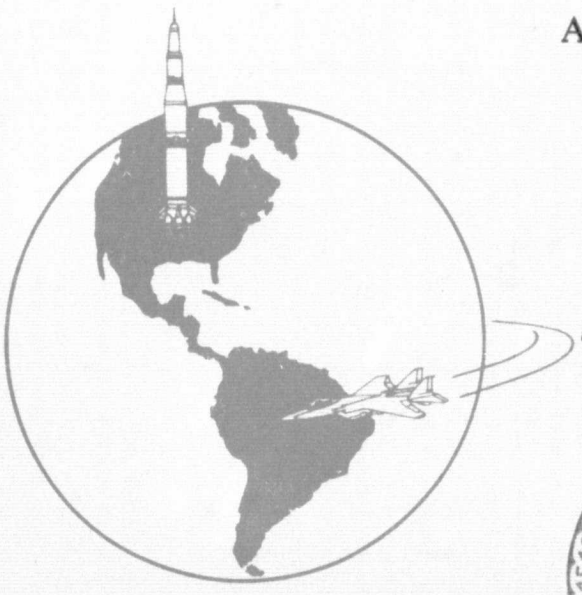

Aerospace Engineering Report 76002

This work was supported by the Johnson Space Center through NASA contract NAS 9—13707

April 1976

Department of Aerospace Engineering and Engineering Mechanics

AN EXPERIMENTAL INVESTIGATION OF SUPERSONIC FLOW PAST A WEDGE-CYLINDER CONFIGURATION*

by

Daniel W. Barnette

Aerospace Engineering Report 76002

*This work was supported by the
Johnson Space Center through NASA Contract NAS 9-13707

Department of Aerospace Engineering and
Engineering Mechanics

The University of Texas at Austin
April 1976

ACKNOWLEDGEMENTS

The research discussed herein was supported by the Johnson Space Center (NASA) through Contract NAS 9-13707. The author gratefully acknowledges the contributions of those who gave their time and efforts in making the research possible. Dr. Winston Goodrich of the Johnson Space Center provided many helpful suggestions. The responsibility of building and partially designing the test model was given to Mr. Henry Franklin, who handled the job superbly. Marilynn McBride assisted in the preparation of the figures. The numerous drafts were cheerfully typed by Mrs. Pat Kleinert and Miss Bernadette Ashman.

The author also expresses his appreciation to Dr. John J. Bertin, of the University of Texas, for reviewing the manuscript and providing technical assistance throughout the program.

TABLE OF CONTENTS

INTRODUCTION

Calculations based on engineering models of the Orbiter entry flow-field, coupled with heat transfer and pressure data from wind tunnel tests, are currently being used to establish methodologies to support vehicle design and trajectory shaping studies. Specifically, the flow-field perturbation which results when the fuselage-generated shock wave interacts with the wing-generated shock wave is particularly important in the design of the Orbiter wing leading-edge. Because of the complexity of the viscid-inviscid interaction phenomena, many experimental investigations of the locally perturbed flow-fields use models consisting of elementary configurations. Using data from an experimental program which employed elementary configurations, Edney (Ref. 1) defined the flow phenomena which characterize the various types of shock-interference patterns. Hains and Keyes (Ref. 2) have categorized the shock-interaction patterns obtained for a variety of Space Shuttle configurations in terms of the flow models of Edney. Bertin, et al (Ref. 3), examined surface-pressure and heat-transfer-rate data for a variety of Shuttle Orbiter configurations over an angle-of-attack range from 0° - 60°. The correlations for these three-dimensional flows indicated that the "type" of shock-interaction pattern was dominated by the effective sweep angle of the leading edge. For the relatively low sweep angles of the straight-wing Orbiters, the interaction between the bow-generated shock wave and the wing-generated shock wave exhibited the characteristics of a Type V shock-interaction pattern. For delta-wing Orbiters, the shock-shock interaction exhibited the characteristics of a Type VI pattern for all angles of attack.

The data discussed above were obtained in facilities where real gas effects would not be expected to significantly alter the shock-interaction

phenomena. By comparing data from facilities using helium, air, nitrogen, and tetrafluoromethane as test gases, Hunt and Creel (Ref. 4) studied the effect of shock-density ratio on the body-shock:wing-shock interaction. The effect of the shock-density ratio, or equivalently the specific heat ratio (gamma), was found to be more significant on the Type V pattern than on the Type VI pattern.

Two numerical codes were developed (Ref. 5) to calculate the two-dimensional flow-field which results when supersonic flow encounters double-wedge configurations. One code used the perfect-gas relations, while the second incorporated a Mollier table to define the equilibrium properties for air. Using the numerical codes described in Ref. 5, both the Type V and the Type VI shock-interaction patterns were found to exist theoretically for a given geometry subject to a given flow condition. Thus, an experimental investigation of supersonic flow past double-wedge configurations was conducted in the University of Texas Supersonic Wind Tunnel (UT SWT). Over the range of geometries tested, it was found that, whereas theoretical solutions both for a Type V pattern and for a Type VI pattern could be generated for a particular flow condition (as defined by the geometry and the free-stream conditions), the weaker, Type VI pattern was observed experimentally (Ref. 6).

As discussed above, the flow-field solutions for the double-wedge configuration in Refs. 5 and 6 are for two-dimensional geometries only. Hence, an investigation was undertaken to develop more rigorous flow-field solutions for the flow along the wing leading-edge. Solutions were developed for the "three-dimensional" flow in the plane of symmetry of a swept cylinder (which represented the wing leading-edge) which was mounted on a wedge (which generated the "bow" shock wave). A numerical code was developed (Ref. 7) using integral techniques to calculate the flow in the shock layer upstream

of the interaction region (i.e., near the wing root). Heat-transfer rates were calculated for various free-stream conditions.

The present investigation was undertaken to examine the effects of crossflow on the resultant flow-field and to verify the flow model used in the theoretical calculations of Ref. 7. Flow-fields were analyzed from schlieren photographs and pressure distributions obtained when a wedge-cylinder configuration was exposed to a supersonic stream at a Mach number of 4.97. The sweep angle of the cylinder was varied from 30° through 70°. The nominal free-stream Reynolds number for the test program was 0.517×10^6/cm (15.7×10^6/ft).

NOMENCLATURE

C_p	local pressure coefficient
$C_{p_{le}}$	experimental value of the pressure coefficient in the plane of symmetry of the cylinder
M	Mach number
p	pressure
r_{le}	radius of the cylinder representing the wing leading-edge
Re	Reynolds number
s	wetted distance (in the z-coordinate direction) measured from the plane of symmetry of the leading edge
w	transverse velocity
x'	distance from the wing root as measured in the plane of symmetry of the leading edge
z	coordinate perpendicular to the plane of symmetry
δ	deflection angle of the inclined wedge
Λ	sweep angle
Λ_s	complement of the sweep angle
ϕ	angle (in radians) measured from the plane of symmetry

Subscripts

∞	free-stream conditions
int	location of interaction-perturbed impingement region in the plane of symmetry of the leading edge

EXPERIMENTAL PROGRAM

Wind Tunnel

The tests were conducted in the University of Texas Supersonic Wind Tunnel (UT SWT). The facility is a two-dimensional, blow-down type wind tunnel which uses air as the test gas. The nominal dimensions of the test section are width 15.2 cm (6.0 in.) by height 17.8 cm (7.0 in.). The test section diverges slightly along its length to allow for boundary layer growth.

The UT SWT accommodates a wide range of stagnation pressures and temperatures. The stagnation pressure test-range for the facility is from 6.89×10^5 to 27.58×10^5 N/m^2 (100 to 400 psi). Stagnation temperatures from 280 to 367°K (505 to 660°R) can be obtained through the use of electric heaters. Still higher stagnation temperatures could be obtained through the use of gas-fired heaters, but they were not used in the present program.

Model

The geometry of the wedge-cylinder configuration used during the present test program is shown in the sketch of Fig. 1 and the photograph of Fig. 2. The dimensions of the model were restricted because of blockage considerations. The wedge, which was 8.26 cm (3.25 in.) in the streamwise direction by 7.42 cm (2.92 in.), was inclined 15° to the free-stream. The value chosen for the wedge deflection angle was sufficient to provide significant variations in pressure along the "wing leading-edge". The "bow" shock wave generated by a 5°-wedge used during a previous program (Ref. 8) was so weak that the pressure along the downstream wedge outboard of the shock interaction was little different than the value near the root region, i.e., inboard of the interaction.

A slab plate with a hemi-cylindrical leading-edge represented the wing leading-edge. The radius of the cylinder was 0.945 cm (0.372 in.); the length, 5.28 cm (2.08 in.). The sweep angle of the cylinder was varied between 30° and 70°.

During the test program a constant gap of 0.178 cm (0.070 in.) was maintained between the wedge and the upstream end of the cylinder to allow for boundary layer bleed off. The gap minimized the possibility of separation in the corner intersection. However, as will be discussed, the effectiveness of the gap diminished at high sweep angles.

A total of 37 static pressure orifices were located on the surfaces of the plate and hemi-cylindrical leading-edge. A majority of the pressure orifices were located in the plane of symmetry of the hemi-cylindrical leading-edge (i.e., the yaw plane of the Shuttle). To evaluate three-dimensional effects (e.g., crossflow), some pressure taps were located off the plane of symmetry of the cylinder at three transverse stations. The specific locations of the pressure orifices are illustrated in Fig. 1 and in Table 1. The orifices located off the plane of symmetry are identified by dual numbers. The initial number identifies the streamwise station (identical to the number of the orifice located in the plane of symmetry at that particular station) while the second integer corresponds to the relative distance from the plane of symmetry for the particular orifice. Sectional views of transverse stations illustrating pressure orifice designations are also shown in Fig. 1.

The coordinates used to locate individual orifices are such that x' represents the distance from the upstream end of the cylinder (i.e., the root of the wing) to a particular pressure orifice located in the plane of symmetry, and s represents the wetted distance as measured from the plane

of symmetry. In Table 1, s has been divided by the radius of the hemi-cylindrical leading-edge. Therefore, the dimensionless value of s/r_{le} for orifices located on the cylinder is equivalent to the angle from the plane of symmetry in radians.

The photograph of Fig. 2 shows a typical setup for the tests. The vertical fin located above the wing leading-edge was used in measuring sweep angles. Pressure leads were taken out of the tunnel floor aft of the model to a mercury-filled manometer board from which static pressure measurements were obtained. Once the mercury levels reached steady state during a run, the pressure leads were sealed (with a knife switch) and the pressures read. Experimental error associated with the visual readings taken from the manometer board corresponds to a pressure error of ± 68.9 N/m^2 (± 0.01 psi).

Test Program

The tests were conducted at a free-stream Mach number of $4.97 \pm .02$. The stagnation pressure was 2.01×10^6 N/m^2 (292 psia) with a maximum fluctuation during a run of $\pm 1.379 \times 10^4$ N/m^2 (± 2 psi). The stagnation temperature of 325°K (585°R) $\pm$ 1.11°K (2.0°R) was controlled through the use of electric heaters, thus reducing the possibility of condensation in the test section. As a result, the nominal free-stream Reynolds number was 0.517×10^6/cm (15.7×10^6/ft). For this Reynolds number, the steady-state test-time is approximately 20 seconds.

Table 2 lists the sweep angle of the "wing leading-edge" corresponding to a particular run. The data consist of schlieren photographs and static wall-pressures.

DISCUSSION OF RESULTS

Previous investigations of the shock-interaction patterns relating to delta-wing Orbiter configurations have shown that the types of shock interactions relevant to the present wedge-cylinder configuration are Type IV, Type V, and Type VI (Ref. 1). Sketches which illustrate the important features of these interaction patterns are presented in Fig. 3. The Type IV pattern, characterized by a supersonic jet impinging on the wing leading-edge, occurs at small angles of sweep. The Type V pattern, which has an impinging shock wave, occurs at intermediate sweep angles. Type VI interference occurs at higher sweep angles and has an impinging expansion fan.

Since the Shuttle Orbiter is a delta-wing configuration, small angles of sweep were not included in the present program. As was noted in the Introduction, the type of shock-interaction pattern which is observed is governed by the sweep angle of the leading edge. Consequently, none of the configurations tested produced a flow-field which exhibited Type IV characteristics. Since the interference patterns encountered for the present program's range of sweep angles were either Type V or Type VI, detailed sketches of the flow-field models for these patterns are presented in Fig. 4. The sketches illustrate the governing flow mechanisms for each pattern. The flow mechanisms of the Type V interaction include:

Region 1 - the undisturbed free-stream flow,

Region 2 - the flow turned through the angle δ by a single weak shock wave,

Region 3 - the flow turned through the deflection angle Λ_s by two weak shock waves,

Region 4 - the relatively high pressure flow which has passed through three shock waves,

Region 5 - the flow which has been processed by two shock waves, with the second shock wave being a strong shock so that the pressure and flow direction matches that of Region 4, at their fluid-fluid interface,

Region 6 - the flow which has passed through a curved shock (i.e., the wing leading-edge shock) such that the shocked flow is subsonic at the upstream end, and

Region 7 - the complex flow downstream of the reflected impinging shock wave.

The Type VI pattern, observed in the higher range of sweep angles, includes:

Region 1 - the undisturbed free-stream flow,

Region 2 - the flow turned through the angle δ by a single weak shock wave,

Region 3 - the flow turned through the deflection angle Λ_S by two weak shock waves,

Region 4 - the flow processed by the left-running expansion waves originating at the intersection of the "bow" shock wave and the wing-root shock wave,

Region 5 - the flow which has passed through the right-running expansion waves associated with the reflection of the centered expansion fan, and

Region 6 - the flow turned by the weak, wing leading-edge shock wave such that the pressure is identical to that in Region 5.

Theoretical predictions of flow-field properties inboard of the interaction region were generated using the numerical code of Ref. 7. Viscous effects

have been neglected in order to maintain simplicity. The code uses a streamtube element method, equating mass flow into the element to the flow out of the element (using an approximate technique to calculate the crossflow). The iterative procedure used to generate the inviscid flow-field solution starts with a two-dimensional shock wave required to turn the flow from Region 2 parallel to the simulated wing leading-edge (i.e., the swept cylinder). When the crossflow is included in the equation for the mass flow for the initial streamtube element, the shock wave relaxes to its three-dimensional value. Because the code models only the flow in Region 3 (i.e., the region immediately downstream of the wing-root shock wave and upstream of the interaction), the code may be used to analyze the flow-field regardless of whether the flow exhibits Type V or Type VI patterns. However, because a weak, two-dimensional shock wave (which is used in the initial iteration) does not exist for relatively low sweep angles, theoretical flow-field solutions can not be obtained for $\Lambda < 39°$ with the present theoretical code even though the resultant three-dimensional wing-root shock wave is weak. Therefore, theoretical solutions are not available for correlation with data from the present experimental program for any Type V pattern and for the Type VI patterns which existed for sweep angles of $\Lambda = 37°$ and $\Lambda = 38°$.

The experimentally-determined pressure distributions from the plane of symmetry have been superimposed on the schlieren photographs. By presenting the data in this manner, it is easier to establish the governing flow mechanisms and their influence on the flow-field. Data are presented for $\Lambda = 30°$ (SC 17), $\Lambda = 45°$ (SC 20), $\Lambda = 55°$ (SC 23), and $\Lambda = 70°$ (SC 26) in Figs. 5a through 5d, respectively. These data are representative of the effect of sweep angle on the flow-field for the range of configurations studied.

Comparison with Figs. 3 and 4a indicates that, for $\Lambda = 30°$ (see Fig. 5a), the interaction is a Type V pattern. Clearly evident are the wing-root shock, the wing leading-edge shock, and the "bow" shock generated by the

wedge. Other elements of the Type V pattern apparent in the photograph are the impinging shock (i.e., the thin, light-colored region immediately below the shock-shock interaction) and the vortex sheet formed by the coalescence of the shear layer and the supersonic jet. Coalescence occurs almost immediately downstream of the interaction region, indicating that Region 5 of Fig. 5a is of limited extent.

Measurements of the shock-wave angle taken from the schlieren photograph of Fig. 5a indicate that the wing-root shock wave is detached at the upstream end of the cylinder (i.e., at the root). Thus, near the wing root, the shock wave is strong and the shocked flow is subsonic. Although the occurrence of a strong shock wave at the root usually indicates that the shock-interaction pattern is Type IV, the generation of a strong shock in this case results when the supersonic flow in Region 2 encounters the "blunt" end of the cylinder. That is, the presence of the gap results in the curved shock at the root of the cylinder. Due to the curvature of the wing-root shock, the flow immediately upstream of the interaction region is supersonic and is, therefore, at a lower pressure than the flow at the wing root. Hence, the flow in Region 3 undergoes an expansion in the streamwise direction. The pressure decrease associated with the resulting acceleration of the flow is apparent from the wing leading-edge pressure measurements for $x' < 2.0\ r_{le}$.

At the downstream end of Region 3, the flow passes through an impinging shock wave generated at the interaction between the bow shock wave and the wing-root shock wave. The impinging shock wave produces the locally high pressure measurement at $x' \approx 2.25\ r_{le}$. Although this high pressure region is typical of Type V interference patterns, the pressure distribution of Fig. 5a represents the one condition encountered in the present test program in which the experimentally-determined pressures exhibited a sudden increase resulting from shock impingement. The inability to measure the high pressures associ-

ated with the impinging shock is a result of the finite spacing of the wing leading-edge pressure orifices. Hence, the limited region affected by the impinging shock (and, therefore, the localized high pressures) could easily be missed. At this sweep angle ($\Lambda = 30°$), the impinging shock is weak, so that the flow along the leading edge remains supersonic in passing into Region 7. This conclusion is based primarily on wave angle measurements of the impinging shock.

Because the flow in Region 7 is supersonic, the impinging shock reflects off the wing leading-edge as a compression wave. The compression wave then intersects the shear layer separating Regions 6 and 7 and is reflected as a series of expansion waves. The resulting multi-reflected expansion waves form the wave pattern observed in Region 7 of Fig. 5a. The pressure decrease associated with the reflected expansion waves is evident in the relatively low pressures measured for x' between 2.5 r_{le} and 4.0 r_{le}.

The strength of the wing leading-edge shock wave (refer to the schlieren photograph of Fig. 5a) is such that the flow at the upstream end of Region 6 (i.e., $x' \approx 2.5\ r_{le}$) is subsonic. Measurements of the local shock-wave angle indicate that, for $x' > 2.75\ r_{le}$, the wing leading-edge shock wave has become weak so that the flow remains supersonic as it passes through the shock wave into Region 6. Thus, the flow accelerates in the spanwise direction. Furthermore, the flow in Region 6 has been processed by one shock wave, whereas the fluid in Region 7 has been subjected to multiple shock waves. Therefore, a shear layer develops between the two regions as a result of the the entropy differential (and the associated velocity differential). Local increases in heat transfer may result as the shear layer approaches the surface (as suggested by Edney, Ref. 1). However, since heat-transfer data were not obtained in the present program, no definite conclusions can be made.

Type VI patterns, typical of those encountered in the present test program, are presented in Figs. 5b, 5c, and 5d. The trace of the wing-root shock wave in the schlieren photographs indicates that the shock is everywhere weak. Hence, the flow remains supersonic throughout Region 3. Mach waves, which are evident in the schlieren photographs, are generated when the supersonic flow is perturbed by the pressure orifices located along the wing leading-edge. The local Mach numbers calculated using these experimentally-observed Mach waves for Region 3 are in reasonable agreement with the theoretical values.

As was noted in the discussion of Figs. 3 and 4, one of the significant features of a Type VI pattern is the impinging expansion fan. For $\Lambda = 45°$ (refer to Fig. 5b), the expansion fan can be seen impinging on the wing leading-edge in the vicinity of $x' = 3.75\ r_{le}$. Also evident in the schlieren photograph is the continuation of the generated "bow" shock wave which extends around the cylinder. This wave can be seen directly above the expansion fan at the downstream end of the cylinder. The reader is reminded that the schlieren photograph is a two-dimensional picture of a three-dimensional flowfield. Thus, the extended "bow" shock wave is not part of the interaction phenomena as it may appear in the photograph. The impinging expansion fan affects only a narrow region of the surface of the cylinder. This will be seen more clearly in Fig. 9b.

Because of the limited extent of the impinging expansion fan and the limited number of pressure orifices, the expansion process cannot be defined experimentally. However, the wing leading-edge pressure distribution does indicate that the flow undergoes a pressure decrease as it accelerates through the expansion fan into Region 5. The pressure measured just downstream of the expansion fan is approximately 0.6 of the pressure measured immediately upstream of the expansion fan. Having been processed by two weak shocks, the flow in Region 3 is at a higher pressure than the flow in Region 6, where the

flow has been processed by one weak shock. Since a free surface (i.e., the shear layer) cannot support a pressure differential, the pressure in Region 6 is identical to the pressure in Region 5. As a result, the flow accelerates along the entire length of the cylinder. Although the pressures and flow direction are identical, an entropy gradient exists between Regions 5 and 6. Hence, a shear layer develops, as observed in Fig. 5b.

As the sweep angle is increased, the expansion fan impinges farther down the wing leading-edge. For $\Lambda = 55°$ (Fig. 5c), the sweep angle is such that the expansion fan passes directly over the downstream end of the cylinder. The expansion, therefore, has no affect on the wing leading-edge pressure distribution. Hence, the pressure distribution is that for Region 3 only.

The data of Fig. 5d are those for $\Lambda = 70°$, which is the maximum sweep angle used in the present program. Because the axis of the cylinder is only slightly inclined relative to the wedge, the complex flow-field is dominated by viscid-inviscid interactions. As indicated in the schlieren photograph, the wedge boundary layer radically affects the flow on the wing leading-edge. As a result, the wing-root shock wave has become completely detached from the wing leading-edge. Also, shock-wave angle measurements indicate that the flow-field properties of Region 3 are little different than those in Region 2. Therefore, the wing-root shock wave generates such small disturbances in the flow-field that its effect is little different from that of an isentropic compression wave. Thus, the pressure is relatively constant along the wing leading-edge, with only a slight decrease in the streamwise direction.

The wing leading-edge pressure distributions of Fig. 5 are presented in a more conventional format in Fig. 6. The experimentally-determined pressure distributions are compared with the theoretical distributions calculated using the code described in Ref. 7. The geometries of the wing-root

shock waves as recorded in the schlieren photographs are compared with the theoretical shock waves in Fig. 7. As has been noted, the theoretical code was unable to generate solutions for sweep angles of $\Lambda < 39°$. Hence, theoretical values are not presented for the pressure distribution of Fig. 6a or the shock wave of Fig. 7a. However, the pressure distribution and the schlieren photograph have been presented for completeness.

The agreement between the theoretical pressures calculated at the wing root of Region 3 and the experimental data is excellent for $\Lambda = 45°$, as shown in the pressure graph of Fig. 6b. For the pressure orifice near the wing root (i.e., $x' = 0.27\ r_{le}$), the experimental pressure is within 1.4% of the theoretical value. For the pressure orifice at the downstream end of Region 3 (i.e., $x' = 3.5\ r_{le}$), the theoretical value underpredicts the experimental data by approximately 18%. The fact that the theoretical pressures are less than the experimental pressures in this region is consistent with the difference in the shock wave traces shown in Fig. 7b. That is, the experimentally-determined trace is at a greater incidence to the flow in region 2 than is the theoretical shock wave trace. Thus, one would expect that the pressures measured on the wing leading-edge would be greater than the theoretical values. The displacement effect of the boundary layer would contribute to this difference, i.e., cause the shock wave to stand off farther from the cylinder than the theoretical shock wave. However, other factors, such as the approximations inherent in the crossflow model, also contribute to the differences between theory and experiment.

The effects of viscid-inviscid interactions become apparent in the wing-root flow-field as the sweep angle is increased. For $\Lambda = 55°$ (refer to Fig. 7c), the schlieren photograph indicates that the effectiveness of the gap has become partially diminished, since the wedge boundary layer interacts with the upstream end of the wing-root shock wave to produce a highly non-

uniform viscous region. Also, an expansion fan originating at the downstream end of the wedge is evident in Fig. 7c. As a result of the combined effects of the expansion fan and the wedge boundary layer, the theoretical pressure distribution presented in Fig. 6c overpredicts the experimental distribution measured at the wing root orifice (i.e., $x' = 0.27\ r_{le}$) by approximately 6%. However, the theoretical pressure at $x' = 3.76\ r_{le}$ is less than the experimental pressure by approximately 18%. As has been discussed previously, the displacement effect of the wing leading-edge boundary layer on the downstream end of the wing-root shock wave contributes to the higher values for the measured pressures.

For the maximum sweep angle considered in the present tests (i.e., $\Lambda = 70°$), there are considerable differences between the theoretical pressures and the experimental pressures, as can be seen in Fig. 6d. Comparison between the theoretical and experimental shock wave trace in the schlieren photograph of Fig. 7d indicates that the viscid-inviscid interactions at the wing root have a marked affect on the stand-off distance of the experimental shock wave. Theoretically, the shock stand-off distance at the wing root is zero. However, as can be seen in the schlieren photograph of Fig. 7d, the measured shock stand-off distance at the wing root is of a finite value. Since viscous effects were not accounted for in the numerical code, the theoretical solution is not expected to reflect the fact that the wing leading-edge flow-field has become seriously altered by the presence of the wedge boundary layer. The theoretical pressure for the orifice nearest the wing root (i.e., $x' = 0.27\ r_{le}$) is approximately 14% higher than the corresponding experimental pressure, whereas the theoretical pressure at $x' = 3.76\ r_{le}$ is approximately 30% lower than the measured value. As a result, the theoretical and experimental distributions at this high sweep angle are significantly different qualitatively as well as quantitatively (see Fig. 6d).

Another dimensionless pressure parameter is the pressure coefficient, C_p. Presented in Fig. 8, therefore, are the wing leading-edge pressure coefficient distributions for the sweep angles considered thus far, i.e., $\Lambda = 30°$ (SC 17), $\Lambda = 45°$ (SC 20), $\Lambda = 55°$ (SC 23), and $\Lambda = 70°$ (SC 26). To gain further insight into the effects of sweep angle on the shock-shock interaction phenomenon, pressure coefficient distributions are presented for three additional sweep angles in Fig. 8. Experimental pressure-coefficient distributions are presented for $\Lambda = 36°$ (SC 37), which is the sweep angle at which the interaction pattern changes from Type V to Type VI, and for $\Lambda = 50°$ (SC 22) and $\Lambda = 60°$ (SC 24), which represent Type VI patterns affected by the upstream boundary layer. The corresponding schlieren photographs are presented in Fig. 9.

The transition from a Type V to a Type VI shock interference pattern is, in general, dependent on the free-stream Mach number and the geometry of the particular configuration used to generate the shock pattern (e.g., double-wedge, wedge-cylinder, etc.). One of the flow-field characteristics indicative of the onset of the Type VI pattern is the weakening of the wing leading-edge shock wave as the sweep angle is increased such that the flow has just become supersonic throughout Region 6 (refer to Fig. 3 and Fig. 4). Wave angle measurements taken from the schlieren photographs (refer to Fig. 9a) and the pressure coefficient distributions taken from the plane of symmetry of the cylinder (refer to Fig. 8e) indicate that, for the present wedge-cylinder configuration, transition from a Type V to a Type VI shock pattern occurs at $\Lambda = 36°$. Hence, for sweep angles of $\Lambda > 36°$, the wing leading-edge flow-field is entirely supersonic (except, of course, in the viscous boundary layer).

It has been observed that, within the intermediate range of sweep angles used in the present test program, theoretical flow-field predictions correlate very well with the experimentally-determined data. However, at higher sweep angles, viscous interactions have a substantial affect on the wing-root

flow-field, resulting in a degradation between theory and experiment. The commencement of the viscous-induced degradation can be seen in the wing leading-edge pressure coefficient distribution for $\Lambda = 50°$ (Fig. 8f). The schlieren photograph corresponding to $\Lambda = 50°$, presented in Fig. 9b, shows that the inclination angle of the cylinder is such that the effects of the wedge boundary layer are just beginning to alter the pressures measured at the wing root. This effect is amplified as the sweep angle is increased, resulting in increasing differences between theoretical values and experimental data. The continuation of the bow shock wave past the cylinder can be easily seen in the schlieren photograph. Since the width (perpendicular to the plane of the photograph) of the bow shock wave is greater than the width of the wing leading-edge shock wave, part of the bow shock wave passes on either side of the cylinder. Thus, what appears to be a shock impingement on the downstream end of the cylinder is in actuality the "superposition effect" resulting from describing the three-dimensional flow-field with a two-dimensional photograph.

The most serious viscous-induced effect on the wing-root flow-field is the result of the expansion fan located at the downstream end of the inclined wedge. Its effect is evident in the pressure coefficient distribution for $\Lambda = 60°$ (Fig. 8g). A local increase in pressure occurs at the upstream end of the cylinder (i.e., $x' = 0.54\ r_{le}$). The pressure coefficient distribution of Fig. 8g indicates that the effects of the wedge expansion fan rapidly diminish downstream of the wing-root orifice. Hence, the pressure for $x' > 0.54\ r_{le}$ follows the general trend typically encountered for the Type VI pattern.

To further determine the effects of sweep, the schlieren photographs have been used to calculate the location of the impingement region on the

simulated wing leading-edge. The impingement locations, denoted as x'_{int}/r_{le}, are presented in Fig. 10 as a function of sweep angle. Also presented in Fig. 10 are the experimentally-determined impingement locations (calculated from schlieren photographs) for a "two-dimensional", double-wedge configuration (Ref. 8). Over the range of sweep angles tested for both the double-wedge and the wedge-cylinder configurations, the location of the interaction-perturbed impingement region moves inboard as the sweep angle decreases. The minimum sweep angle for which a Type VI shock pattern occurs for the double-wedge configuration is approximately 11° higher than for the wedge-cylinder configuration. Since crossflow effects are virtually non-existent for the double-wedge configuration, the stand-off distance of the wing leading-edge shock wave is greater than that for the cylindrical leading-edge. Therefore, this shock wave is stronger for the two-dimensional flow-field. Hence, the minimum sweep angle for which supersonic flow is maintained throughout the leading edge flow-field (which corresponds to a Type VI shock pattern) is expected to be higher for the double-wedge configuration.

It is evident from the data of Fig. 10 that the location of the interaction region for the two-dimensional flow is inboard of the corresponding location for the wedge-cylinder configuration. Furthermore, whereas the interaction location is an approximately linear function of sweep angle for the double-wedge configuration, such is not the case for the wedge-cylinder. To see why the double-wedge and the wedge-cylinder configurations produce widely varying impingement locations, the interaction region of the bow shock wave and the wing-root shock wave must be considered. Schlieren photographs were used to prepare the sketches (refer to Fig. 11) of the shock patterns generated by these two configurations. The deflection angle is $\Lambda_s = 45°$ for these sketches. The shock patterns for the double-wedge

(Fig. 11a) and the wedge-cylinder (Fig. 11b) have been superimposed in Fig. 11c in order to compare the regions of impingement. In the two-dimensional flow-field of the double-wedge configuration (refer to Fig. 11a), the wing-root shock is linear. Furthermore, since crossflow effects are negligible for the double-wedge, the stand-off distance of the two-dimensional wing-root shock is greater than the corresponding "three-dimensional" value for the swept cylinder at the same sweep angle. Since, for identical free-stream Mach numbers, the bow shock-wave angle is the same for both configurations, the intersection of the wing-root shock and the bow shock will occur nearer the wing-root for the double-wedge. In addition, the root region Mach number is lower for the two-dimensional flow, and so the impinging expansion waves are steeper. As a result of the relationship between the impingement phenomenon and the shock-shock interaction, the impingement region for the two-dimensional case will also be nearer the wing-root. As is the case for the wedge-cylinder (refer to Fig. 11b), the existence of crossflow on the wing leading-edge results in a curved wing-root shock. Therefore, the shock-shock interaction, and hence the impingement location is not expected to vary linearly as the sweep angle is varied for the swept cylinder.

An assumption basic to the theoretical flow-field model was that the transverse velocity (i.e., the crossflow velocity) associated with a particular streamtube element could be calculated using the linear approximation:

$$w = \frac{dw}{dz} \Delta z$$

This approximation further assumed that the variation of the pressure in a circumferential direction obeys the "modified Newtonian relation":

$$C_p = C_{p_{le}} \cos^2 \phi$$

where C_p is the local pressure coefficient, ϕ is the displacement angle from the plane of symmetry (and equal to s/r_{le} - refer to Fig. 1), and $C_{p_{le}}$ is the pressure coefficient for the plane of symmetry of the wing leading-edge at the location of interest. For the numerical code described in Ref. 7, $C_{p_{le}}$ is the theoretical pressure coefficient calculated using the static pressure determined from the streamtube element analysis. The experimentally-determined circumferential pressure coefficients are compared with the Newtonian "correlations" in Fig. 12 for the test runs discussed previously: $\Lambda = 30°$ (SC 17), $\Lambda = 36°$ (SC 37), $\Lambda = 45°$ (SC 20), $\Lambda = 50°$ (SC 22), $\Lambda = 55°$ (SC 23), $\Lambda = 60°$ (SC 24), and $\Lambda = 70°$ (SC 26). For the correlation curves presented in Fig. 12, $C_{p_{le}}$ is the experimental value of the pressure coefficient determined from the static pressure measured at the location of interest in the plane of symmetry. Hence, as evident in Fig. 12, the correlation between "theory" and the data is automatically satisfied when ϕ (or s) is zero. Thus, the agreement between the experimental data and the correlation for the pressures merely indicates that the modified Newtonian model provides a reasonable representation of the pressure variation near the plane of symmetry. There may still exist variations between the actual crossflow velocity and the theoretical value which uses the theoretical values for the pressure in the plane of symmetry.

Since pressure taps are located at three transverse stations on the cylinder (see Fig. 1), each test run produced three sets of data with which the Newtonian values of the pressure coefficient can be correlated. The correlation between a particular set of experimental data and the corresponding Newtonian distribution is partly dependent on the sweep angle of the wing leading-edge. For relatively low sweep angles, the experimentally-determined pressure coefficients are in good agreement with the calculated

values. The data obtained for $\Lambda = 30°$ (refer to Fig. 12a) indicate that, at $s = 0.262\ r_{le}$, the calculated pressure coefficients for each transverse station are within 4% of the measured pressure coefficients, whereas, for $s = 0.524\ r_{le}$, the Newtonian distributions are within 10% of the experimental pressure coefficients. The Newtonian flow assumption also exhibits good agreement with experimental data within the intermediate range of sweep angles. As shown for $\Lambda = 50°$ (Fig. 12d), the maximum deviation encountered at $s = 0.262\ r_{le}$ corresponds to a difference between theory and experiment of approximately 2%. For $s = 0.524\ r_{le}$, the theoretical distributions underpredict the experimental values by approximately 13%. For the relatively high sweep angles, the local flow at the orifices farther from the plane of symmetry is often disturbed by the support system for the tunnel model. Therefore, correlation between these data and the Newtonian relation is meaningless.

CONCLUDING REMARKS

An experimental program has been conducted to investigate the flow-field properties inboard of the shock interaction in order to develop a theoretical flow model. Based on correlations between experimental data and theoretical calculations using a streamtube element method, the following conclusions are made.

1) Due to the inability of the code to generate an initial solution to the corresponding two-dimensional flow-field, theoretical calculations are not available for $\Lambda < 39°$.

2) Within the intermediate range of sweep angles studied in the present test program, theoretical predictions are in excellent agreement with experimental data obtained at the upstream end of the wing-root region. Discrepancies between theory and experiment at the downstream end of the wing-root region are attributable (in part) to displacement effects induced on the flow-field by the wing leading-edge boundary layer.

3) At relatively high sweep angles, the viscid-inviscid interactions generated by the wedge boundary layer dominate the wing leading-edge flow-field. As a result, the validity of the calculated flow-field properties is reduced at higher sweep angles.

REFERENCES

1. Edney, B.: "Anomalous Heat Transfer and Pressure Distributions on Blunt Bodies at Hypersonic Speeds in the Presence of an Impinging Shock", Report 115, 1968, Flygtechniska Forsoksanstalten (The Aeronautical Research Institute of Sweden), Stockholm.

2. Hains, F.D., and Keyes, J.W.: "Shock Interference Heating in Hypersonic Flows", AIAA Journal, Vol. 10, No. 11, November 1972, pp. 1441-1447.

3. Bertin, J.J., Graumann, B.W., and Goodrich, W.D.: "Aerothermodynamic Aspects of Shock-Interference Patterns for Shuttle Configurations During Entry", AIAA Paper 73-238, Washington, D.C., 1973.

4. Hunt, J.L., and Creel, T.R., Jr.: "Shock-Interference Heating and Density-Ratio Effects, Pt. II: Hypersonic Density-Ratio Effect", NASA Space Shuttle Technology Conference, Vol. I: Aerothermodynamics, Configurations and Flight Mechanics, TMX-2272, April 1971, NASA.

5. Bertin, J.J., Graumann, B.W., and Goodrich, W.D.: "High Velocity and Real-Gas Effects on Weak Two-Dimensional Shock-Interaction Patterns", Journal of Spacecraft and Rockets, Vol. 12, No. 3, March 1975, pp. 155-161.

6. Bertin, J.J., and Hinkle, J.C.: "Experimental Investigation of Supersonic Flow Past Double-Wedge Configurations", AIAA Journal, July 1975, Vol. 13, No. 7, pp. 897-901.

7. Bertin, J.J., Mosso, S.J., Barnette, D.W., and Goodrich, W.D.: "Engineering Flow Fields and Heating Rates for Highly-Swept Wing Leading-Edges", Accepted for publication in the Journal of Spacecraft and Rockets.

8. Bertin, J.J., and Hinkle, J.C.: "An Experimental Investigation of the Flow-Field for Double-Wedge Configurations in a Mach 4.97 Stream", Aerospace Engineering Report 74003, June 1974, The University of Texas at Austin.

Table 1. - Location of Static-Pressure Orifices

Orifice No.	x' cm (in.)	$\frac{x'}{r_{le}}$	$\frac{s}{r_{le}}$
1	.254 (0.10)	0.269	0.0
2	.508 (0.20)	0.538	0.0
3	.762 (0.30)	0.806	0.0
4	1.016 (0.40)	1.075	0.0
5	1.270 (0.50)	1.344	0.0
6	1.524 (0.60)	1.613	0.0
7	1.778 (0.70)	1.882	0.0
8	2.032 (0.80)	2.151	0.0
9	2.286 (0.90)	2.419	0.0
10	2.540 (1.00)	2.688	0.0
11	2.794 (1.10)	2.957	0.0
12	3.048 (1.20)	3.226	0.0
13	3.302 (1.30)	3.495	0.0
14	3.556 (1.40)	3.763	0.0
15	3.810 (1.50)	4.032	0.0
16	4.064 (1.60)	4.301	0.0
17	4.318 (1.70)	4.570	0.0
18	4.572 (1.80)	4.839	0.0
19	4.826 (1.90)	5.108	0.0
20	5.080 (2.00)	5.376	0.0
5-1	1.270 (0.50)	1.344	0.785
5-2	1.270 (0.50)	1.344	0.262
5-3	1.270 (0.50)	1.344	0.524
5-4	1.270 (0.50)	1.344	1.047
5-5	1.270 (0.50)	1.344	1.571
5-6	1.270 (0.50)	1.344	2.563
10-1	2.540 (1.00)	2.688	0.785
10-2	2.540 (1.00)	2.688	0.262
10-3	2.540 (1.00)	2.688	0.524
10-4	2.540 (1.00)	2.688	1.047

Table 1. - Continued

Orifice No.	x' cm (in.)	$\frac{x'}{r_{le}}$	$\frac{s}{r_{le}}$
10-5	2.540 (1.00)	2.688	1.571
15-1	3.810 (1.50)	4.032	0.785
15-2	3.810 (1.50)	4.032	0.262
15-3	3.810 (1.50)	4.032	0.524
15-4	3.810 (1.50)	4.032	1.047
15-5	3.810 (1.50)	4.032	1.571
15-6	3.810 (1.50)	4.032	2.563

Table 2. - Schedule of Test Runs in which Static Pressures were Measured

$M_\infty = 4.97$ $\delta = 15°$ $R_{e_\infty} = .517 \times 10^6$/cm ($15.7 \times 10^6$/ft)

$\Lambda = 30°$ SC 17	$\Lambda = 45°$ SC 20
$\Lambda = 35°$ SC 18	$\Lambda = 50°$ SC 22
$\Lambda = 36°$ SC 37	$\Lambda = 55°$ SC 23
$\Lambda = 37°$ SC 38	$\Lambda = 60°$ SC 24
$\Lambda = 38°$ SC 40	$\Lambda = 65°$ SC 25
$\Lambda = 39°$ SC 41	$\Lambda = 70°$ SC 26
$\Lambda = 40°$ SC 19	

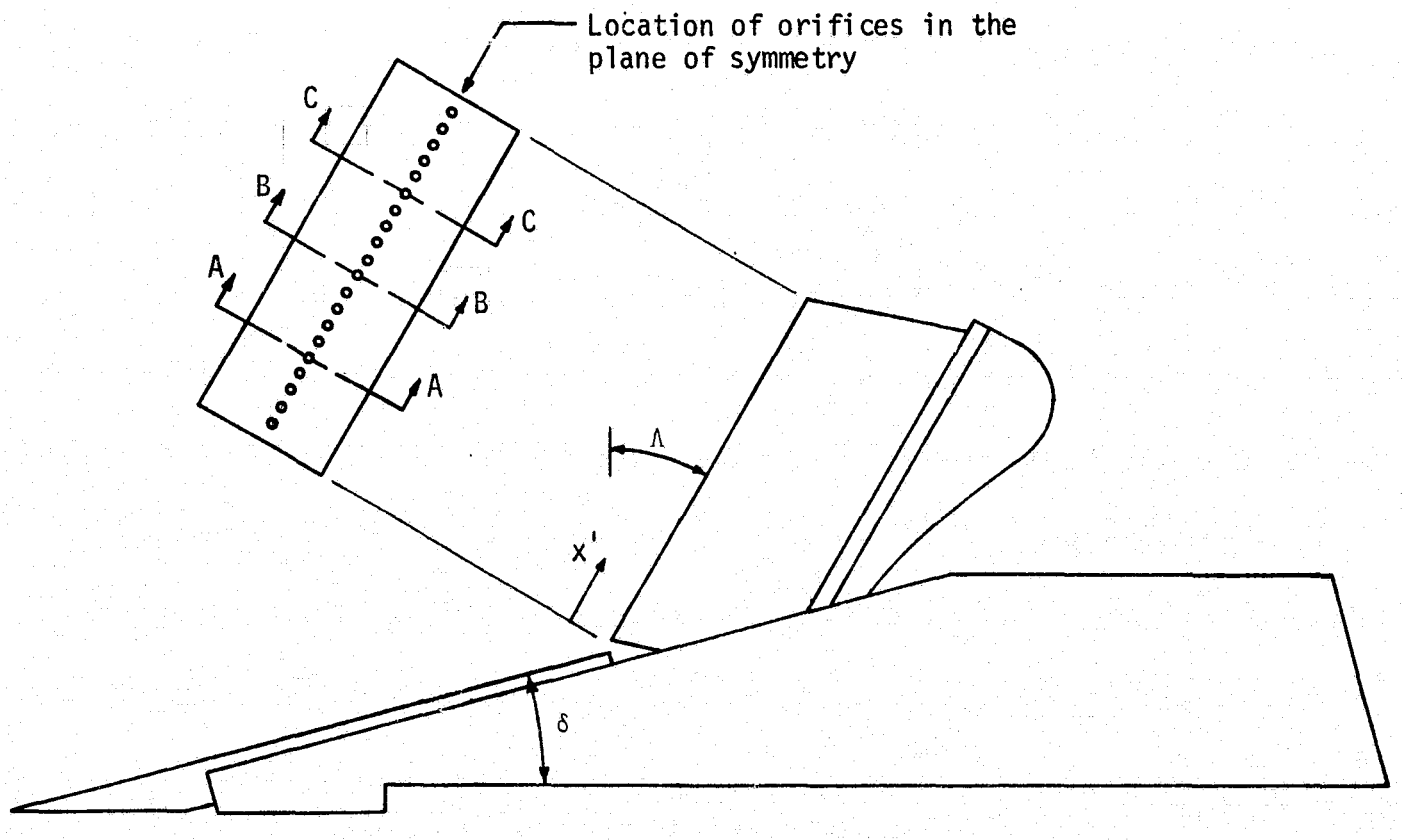

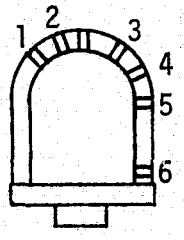

Section A-A
"5-" series

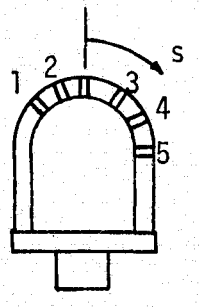

Section B-B
"10-" series

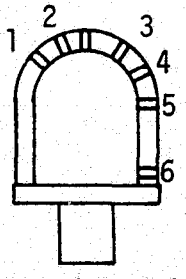

Section C-C
"15-" series

Figure 1. - Sketch of wedge-cylinder model illustrating pressure orifices located off the plane of symmetry.

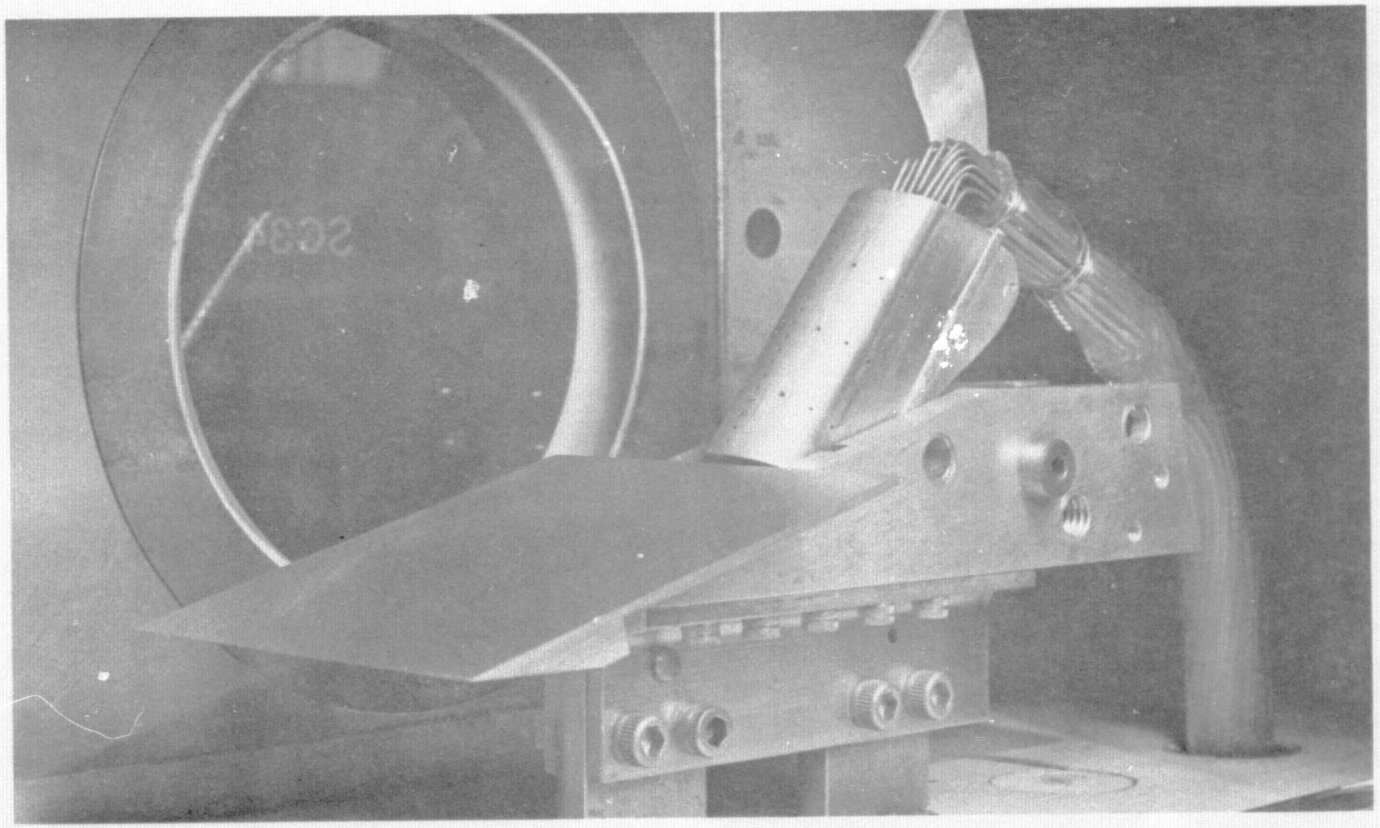

Figure 2. - Wedge-cylinder configuration used in the UT SWT test program.

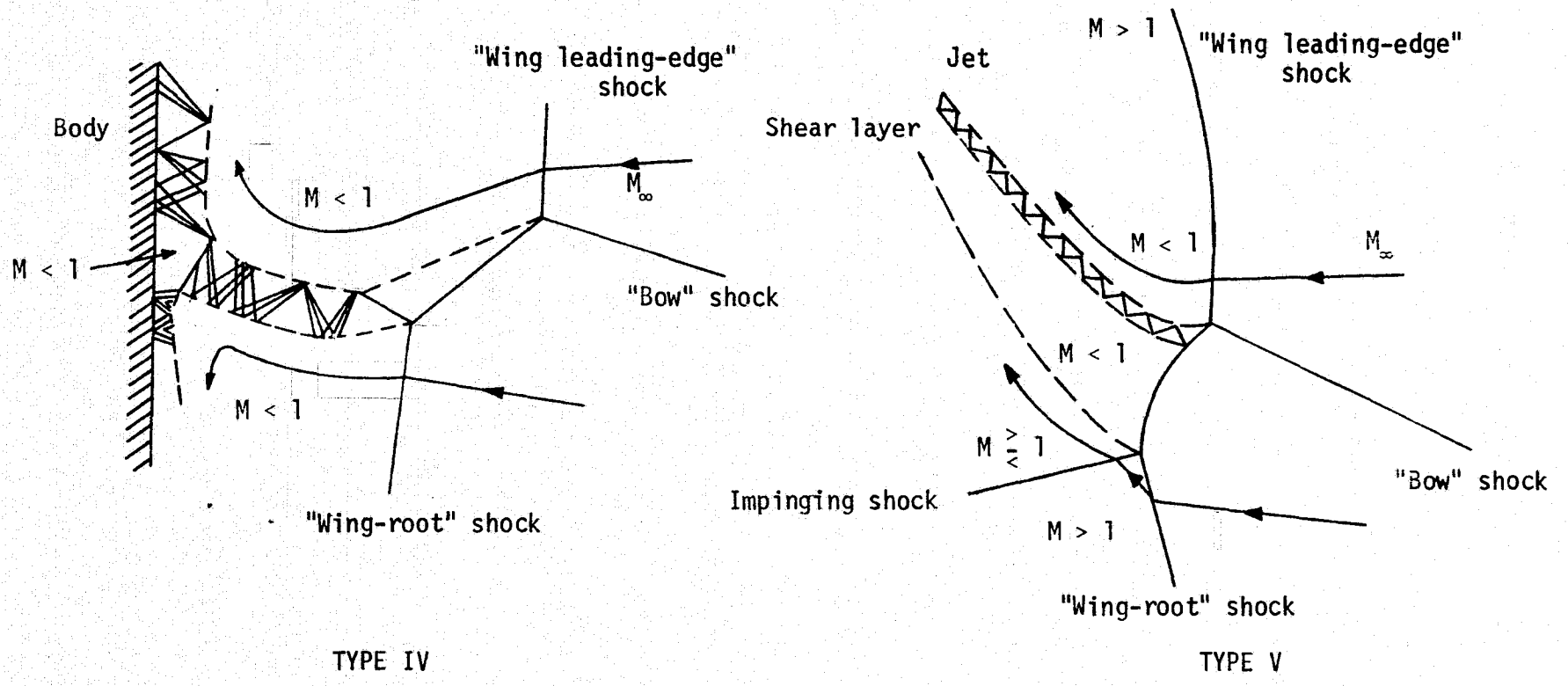

(a)

Figure 3. - Sketch of shock-interference patterns as given by Edney (Ref. 1).

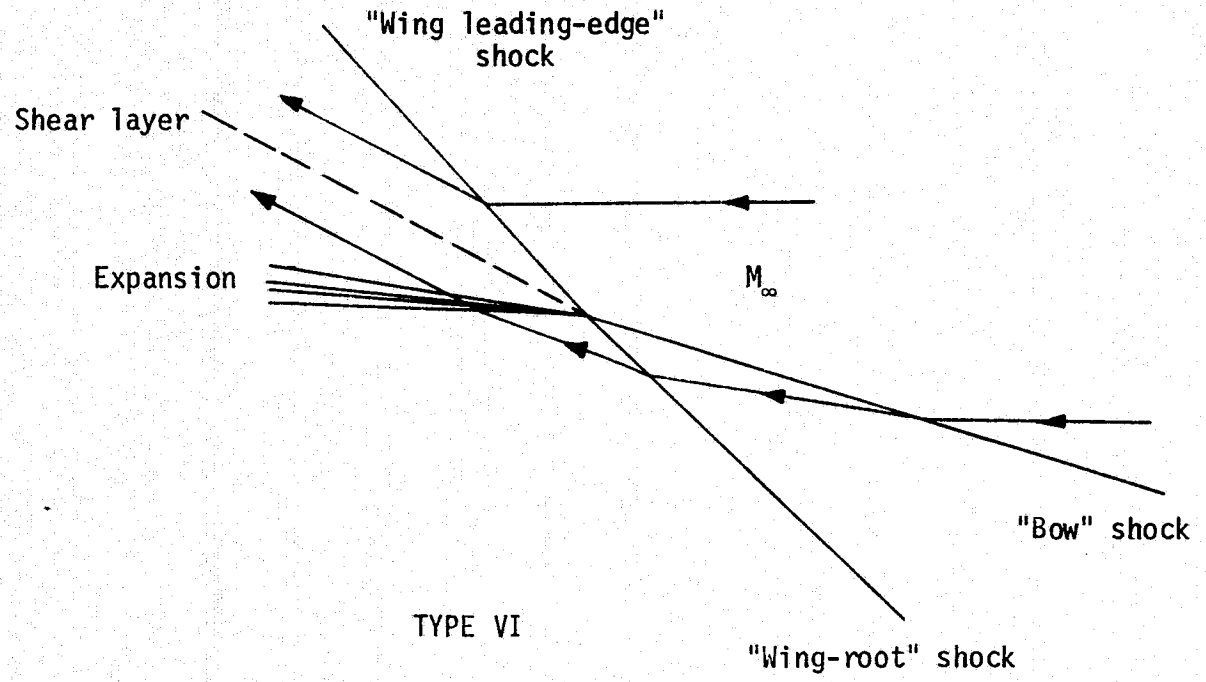

(b)

Figure 3. - Concluded.

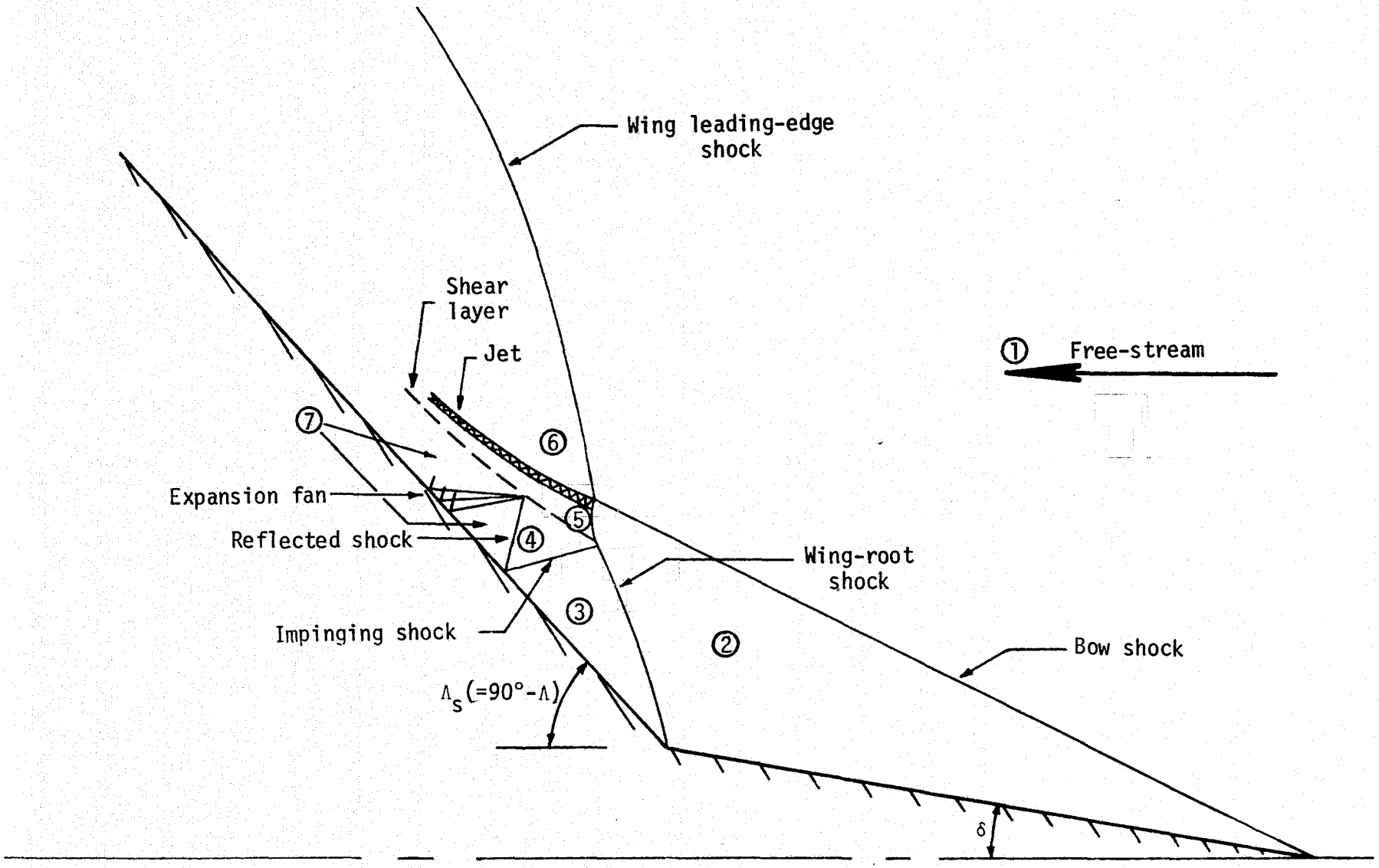

(a) Type V

Figure 4. - Flow models of the shock-interaction pattern for a wedge-cylinder (not to scale).

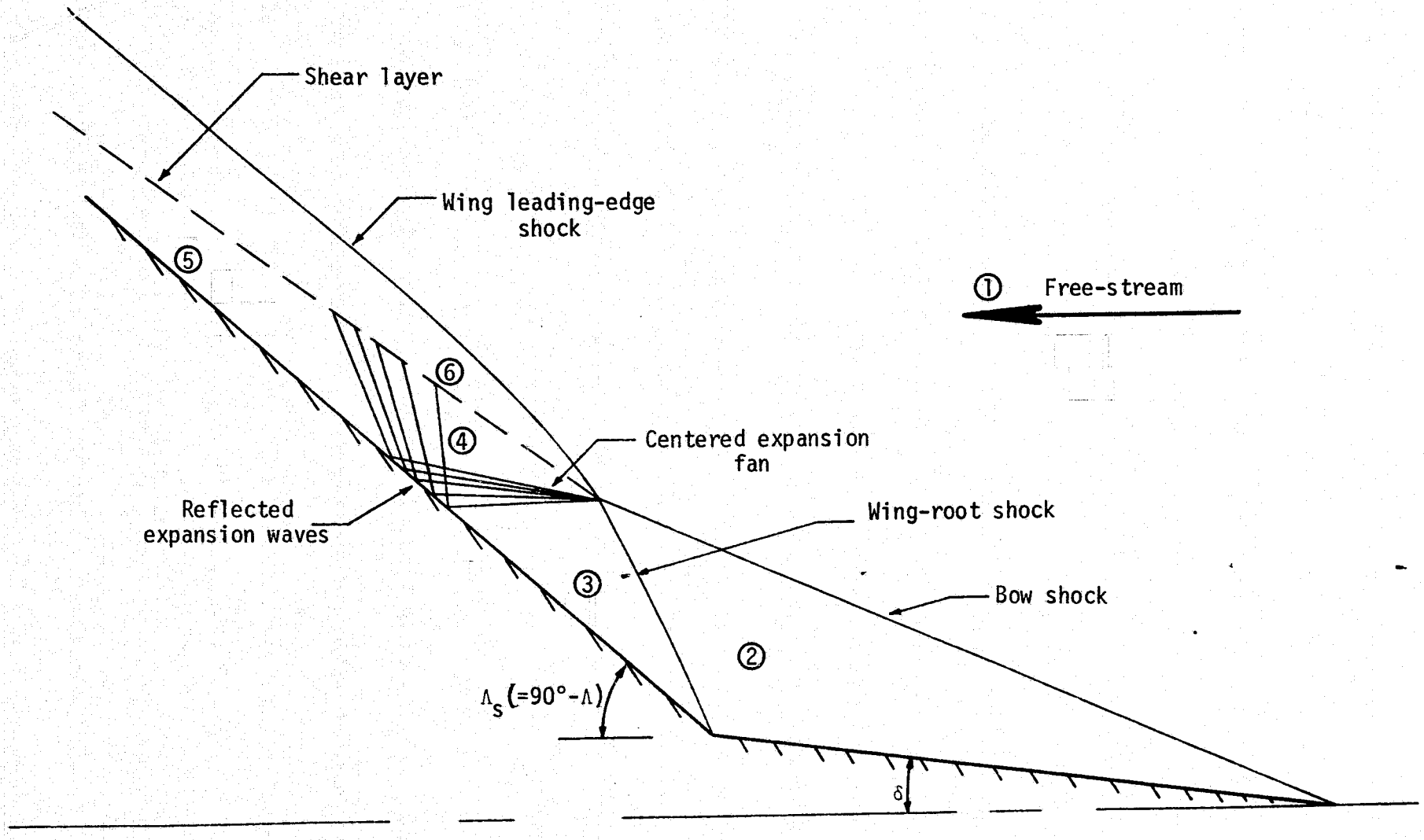

(b) Type VI

Figure 4. - Concluded.

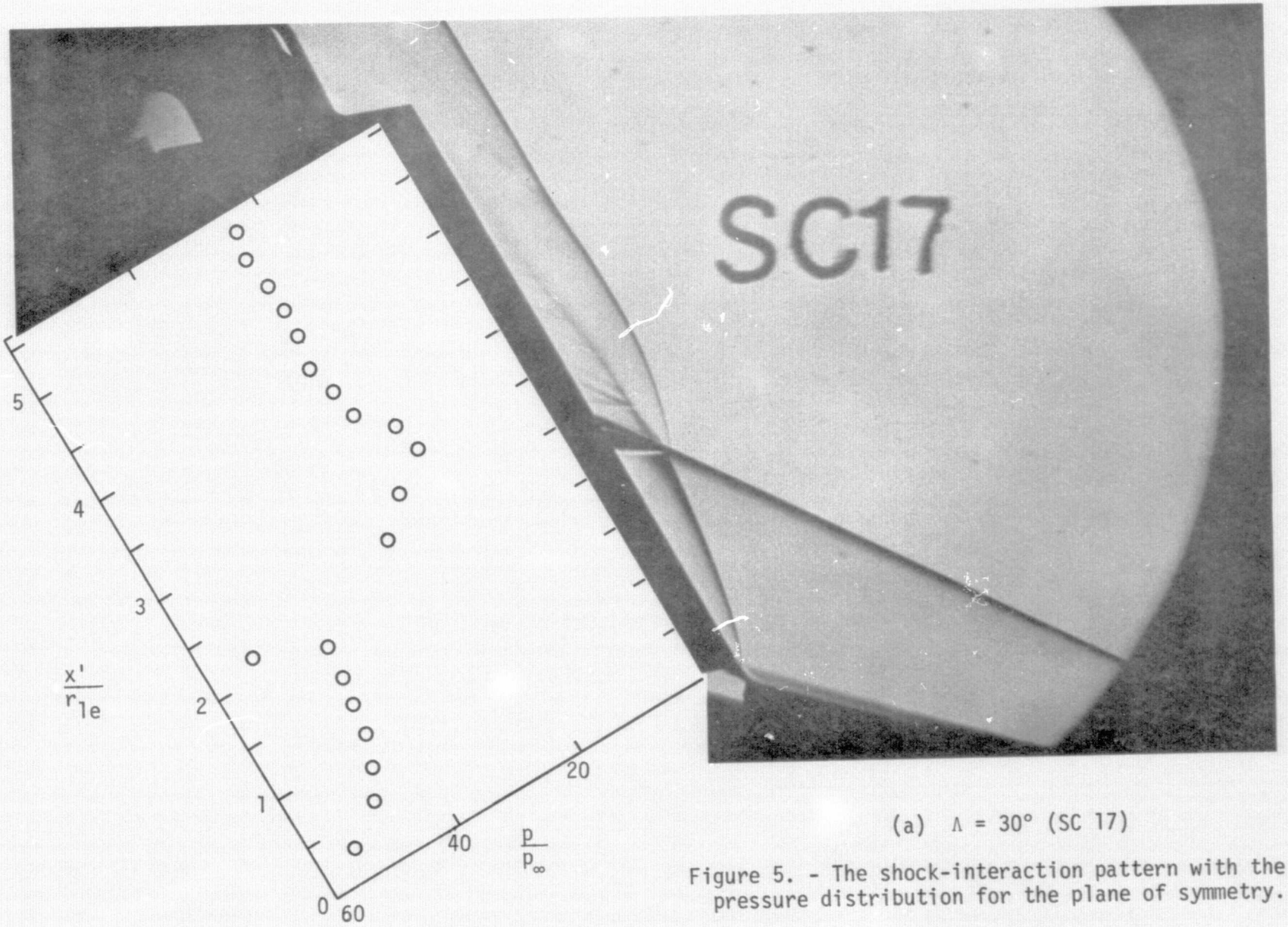

(a) $\Lambda = 30°$ (SC 17)

Figure 5. - The shock-interaction pattern with the pressure distribution for the plane of symmetry.

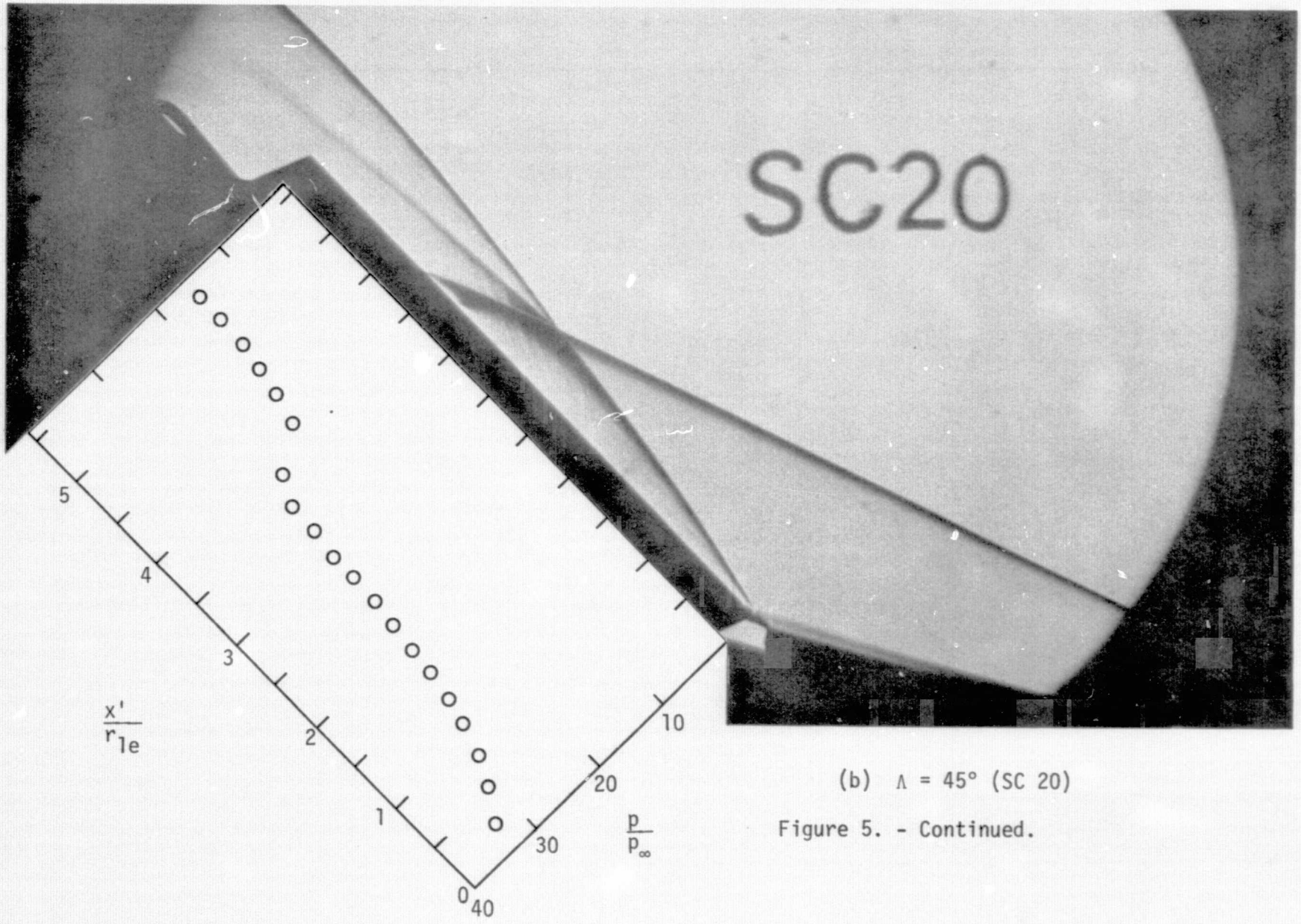

(b) $\Lambda = 45°$ (SC 20)

Figure 5. - Continued.

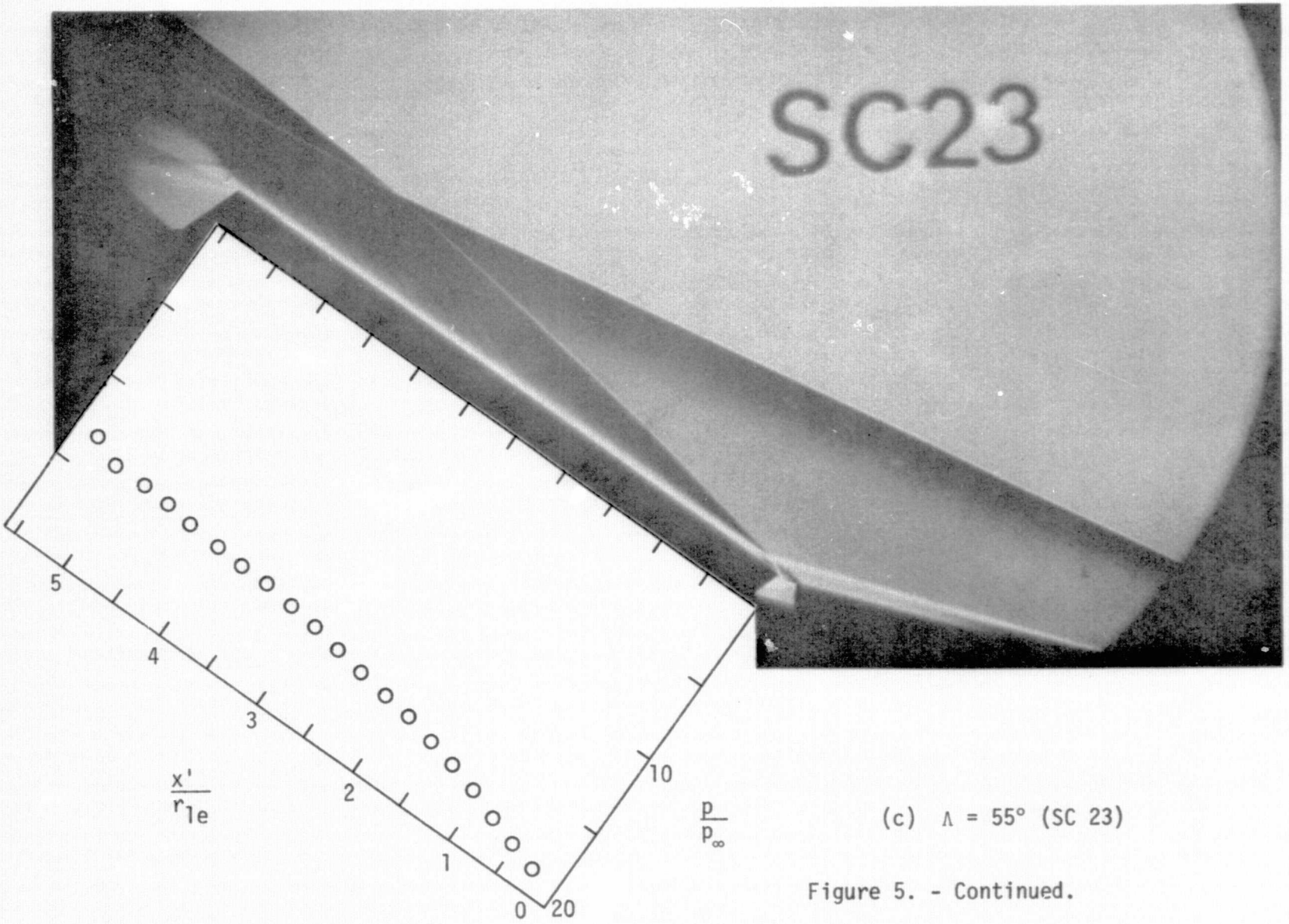

(c) $\Lambda = 55°$ (SC 23)

Figure 5. - Continued.

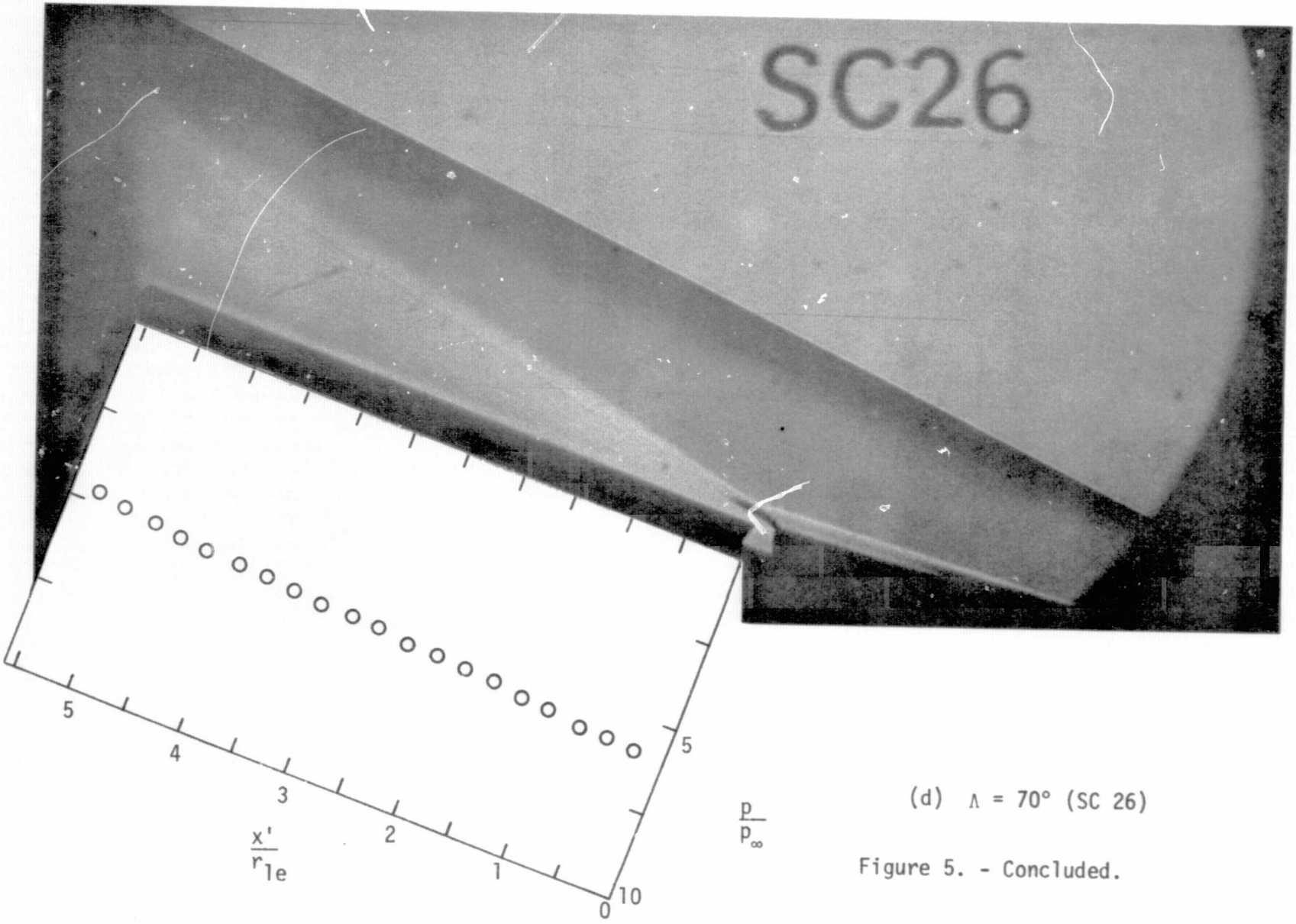

(d) $\Lambda = 70°$ (SC 26)

Figure 5. - Concluded.

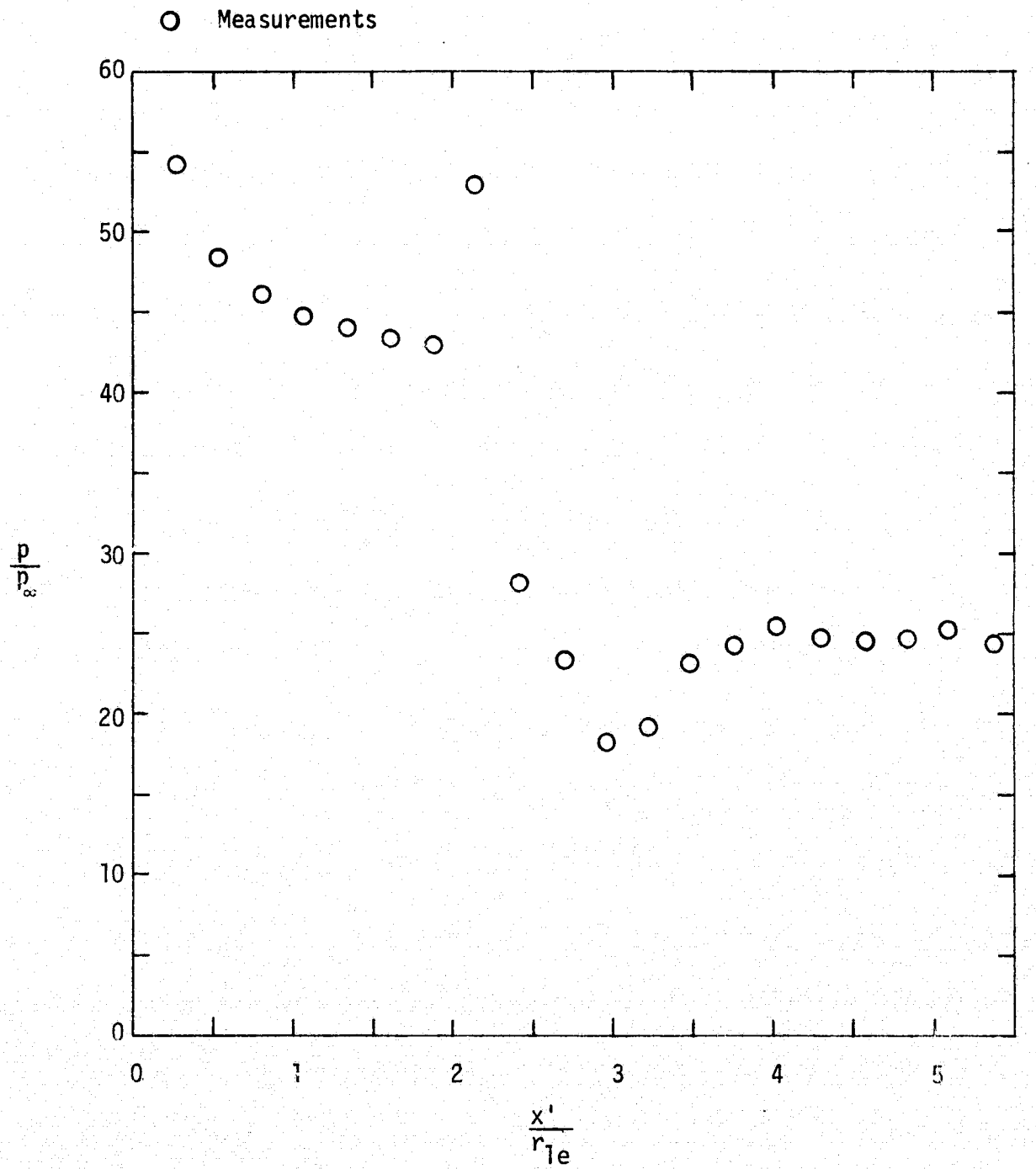

(a) $\Lambda = 30°$ (SC 17)

Figure 6. - Comparison of the theoretical and the experimental pressure distributions in the plane of symmetry of the cylinder.

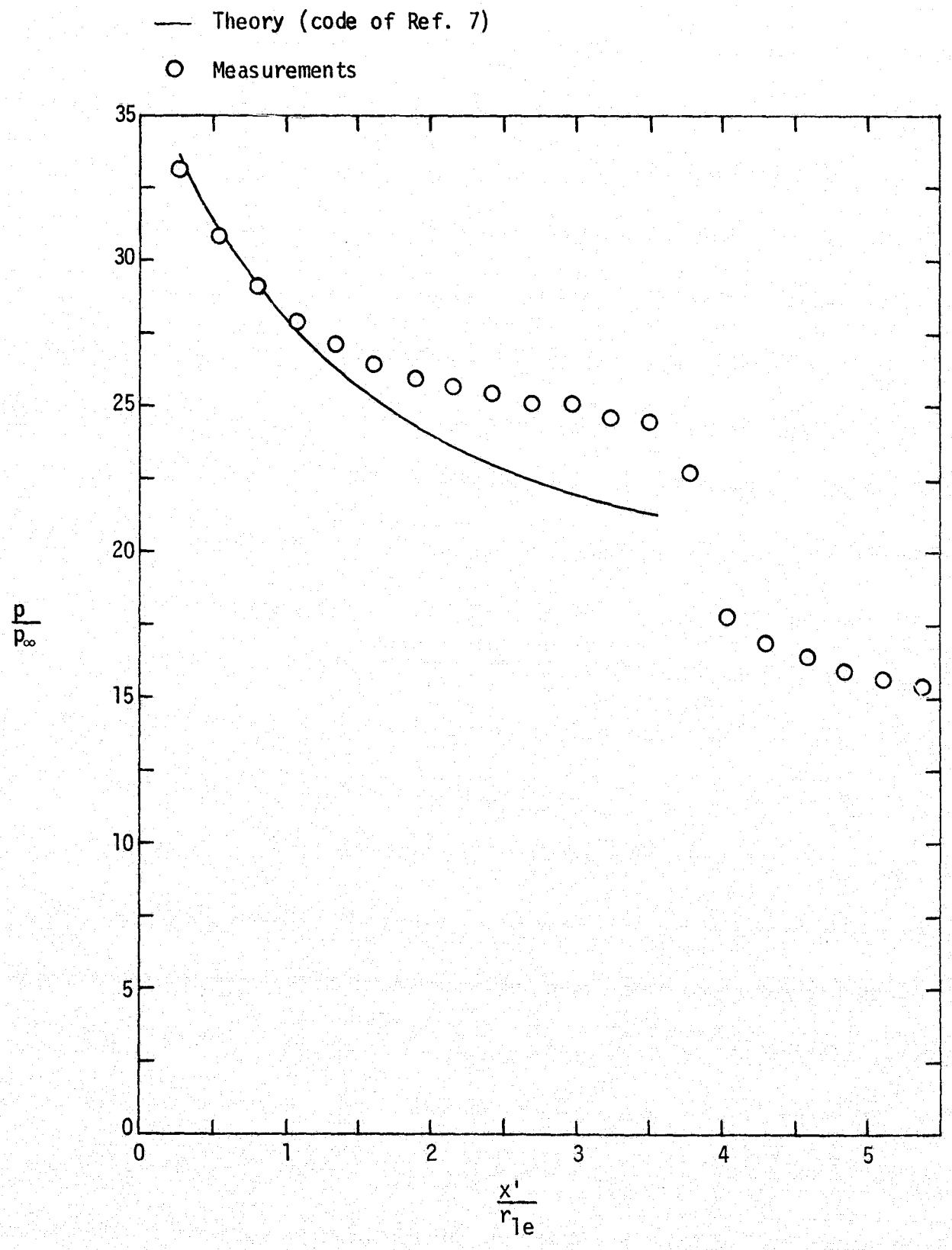

(b) $\Lambda = 45°$ (SC 20)

Figure 6. - Continued.

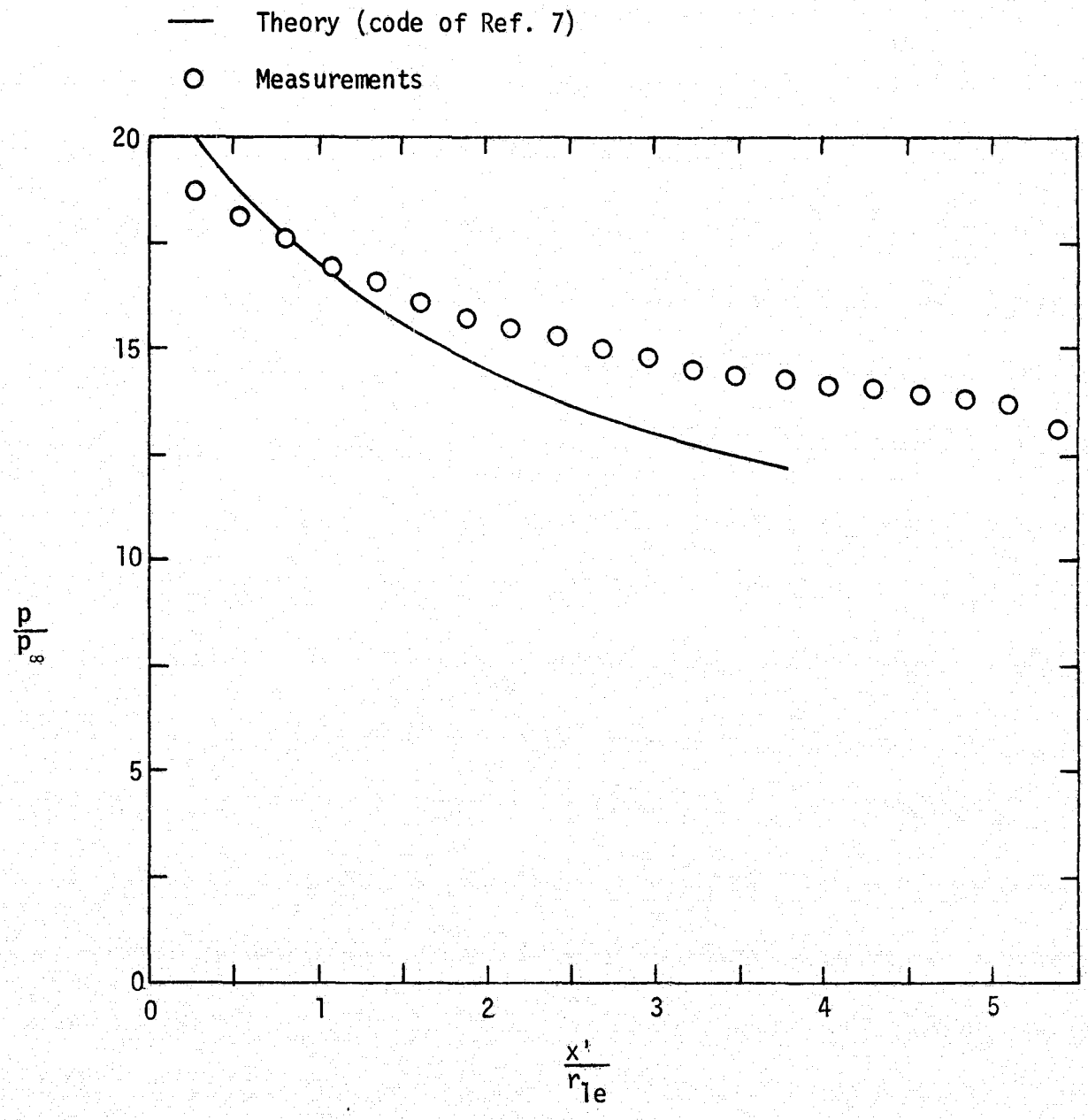

(c) $\Lambda = 55°$ (SC 23)

Figure 6. - Continued.

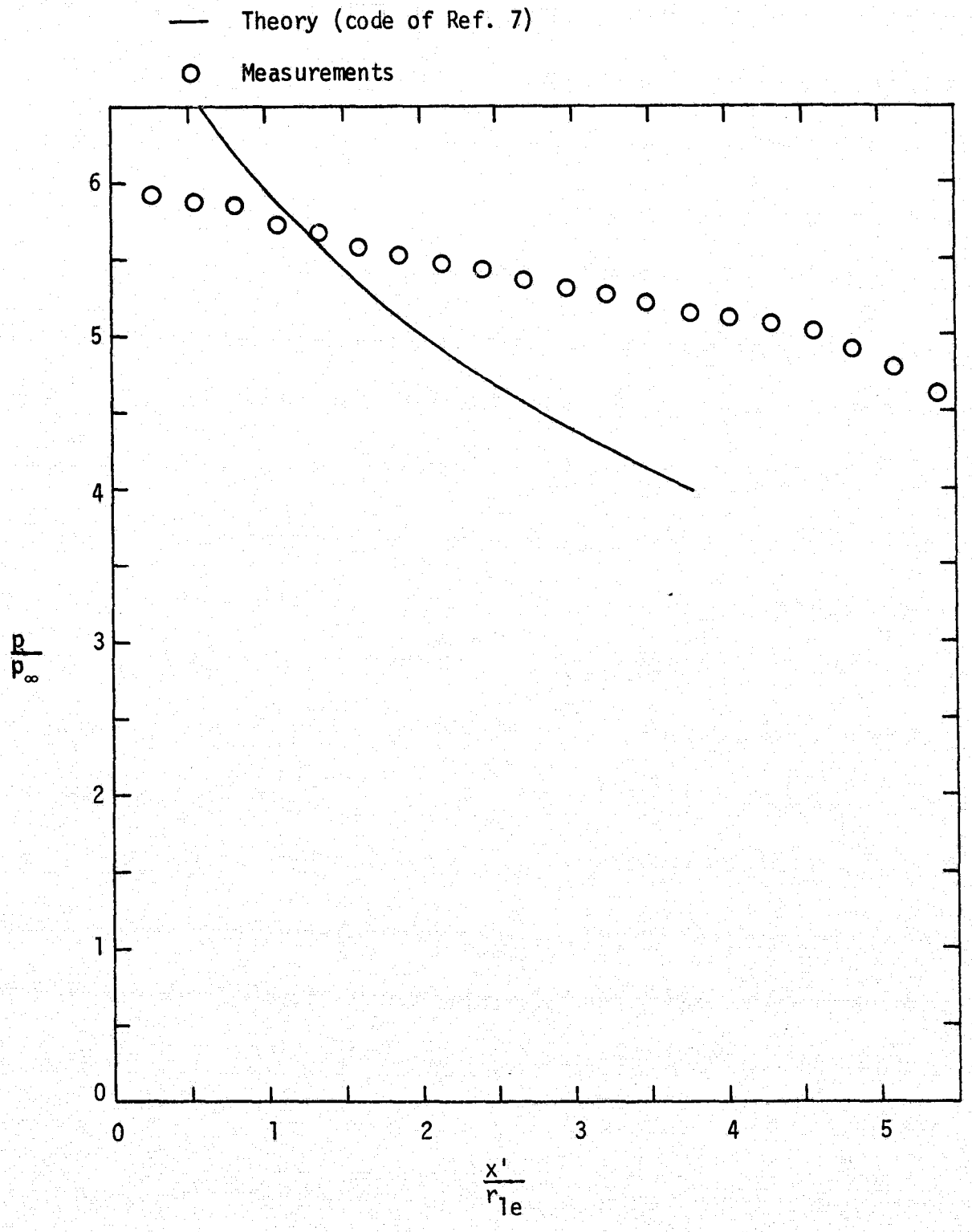

(d) $\Lambda = 70°$ (SC 26)

Figure 6. - Concluded.

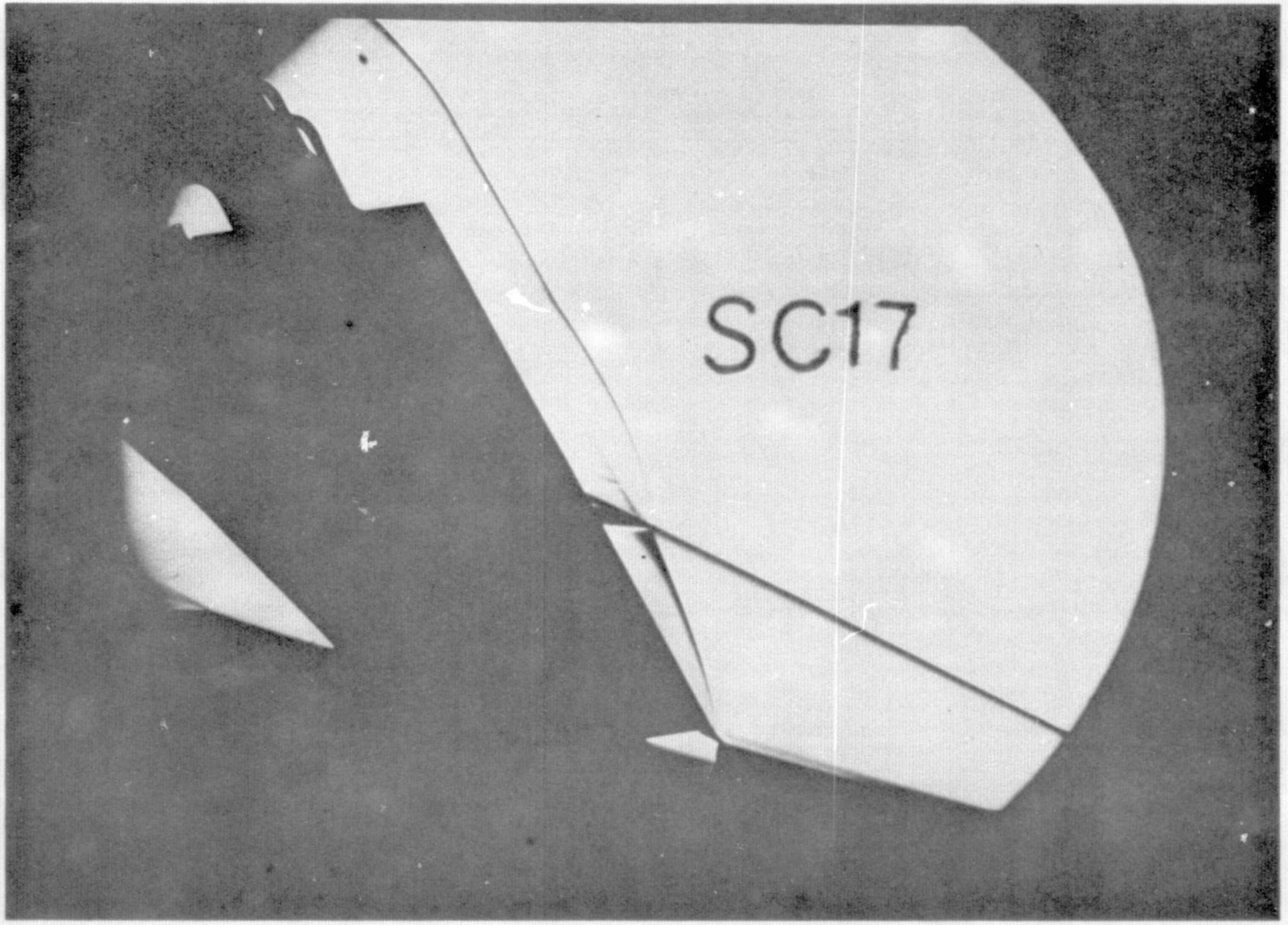

(a) $\Lambda = 30°$ (SC 17)

Figure 7. - A comparison of the experimental and the theoretical wing-root shock wave. Theoretical location of the wing-root shock wave is indicated by the symbol O.

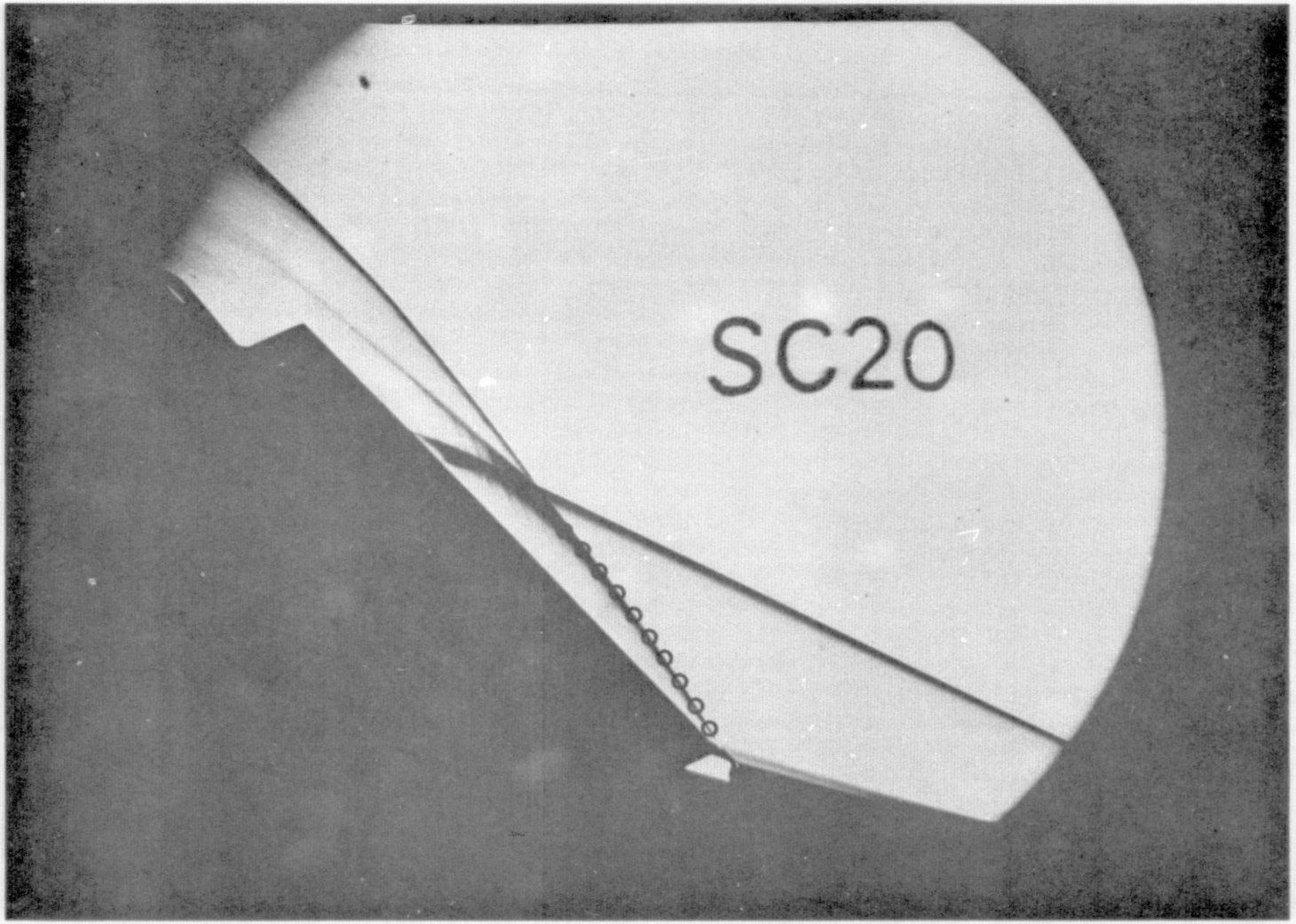

(b) $\Lambda = 45°$ (SC 20)

Figure 7. - Continued.

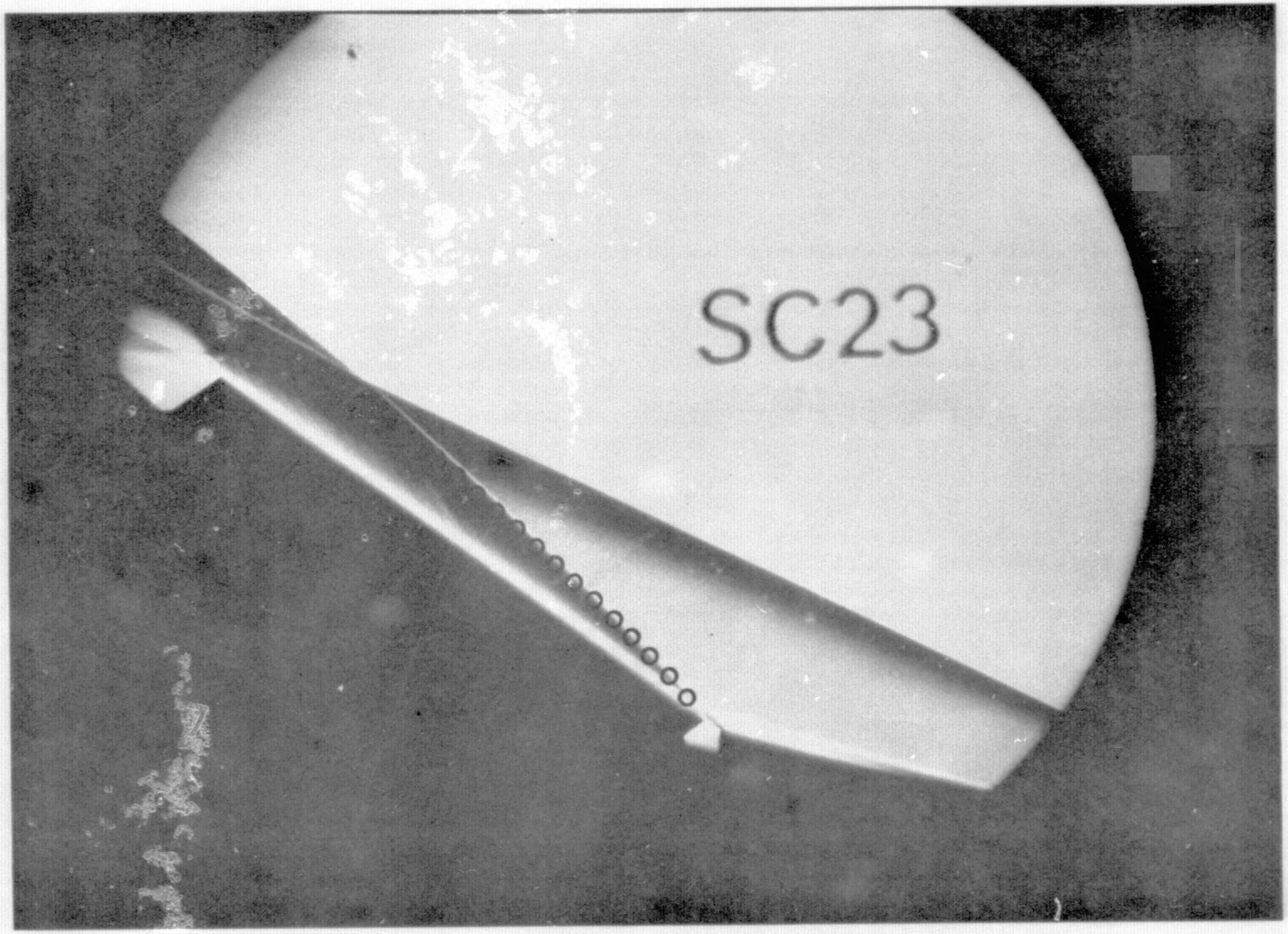

(c) Λ = 55° (SC 23)

Figure 7. - Continued.

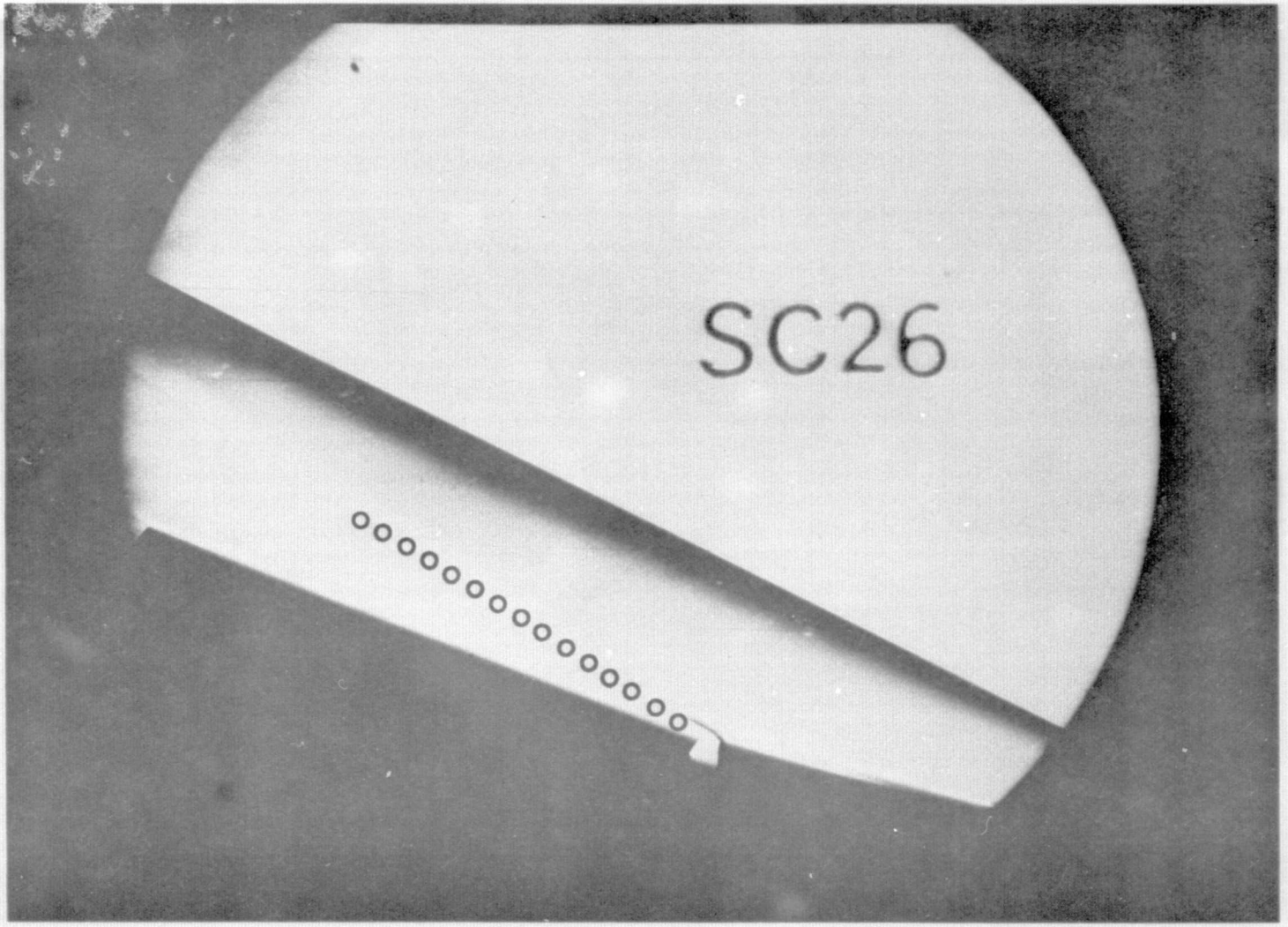

(d) $\Lambda = 70°$ (SC 26)

Figure 7. - Concluded.

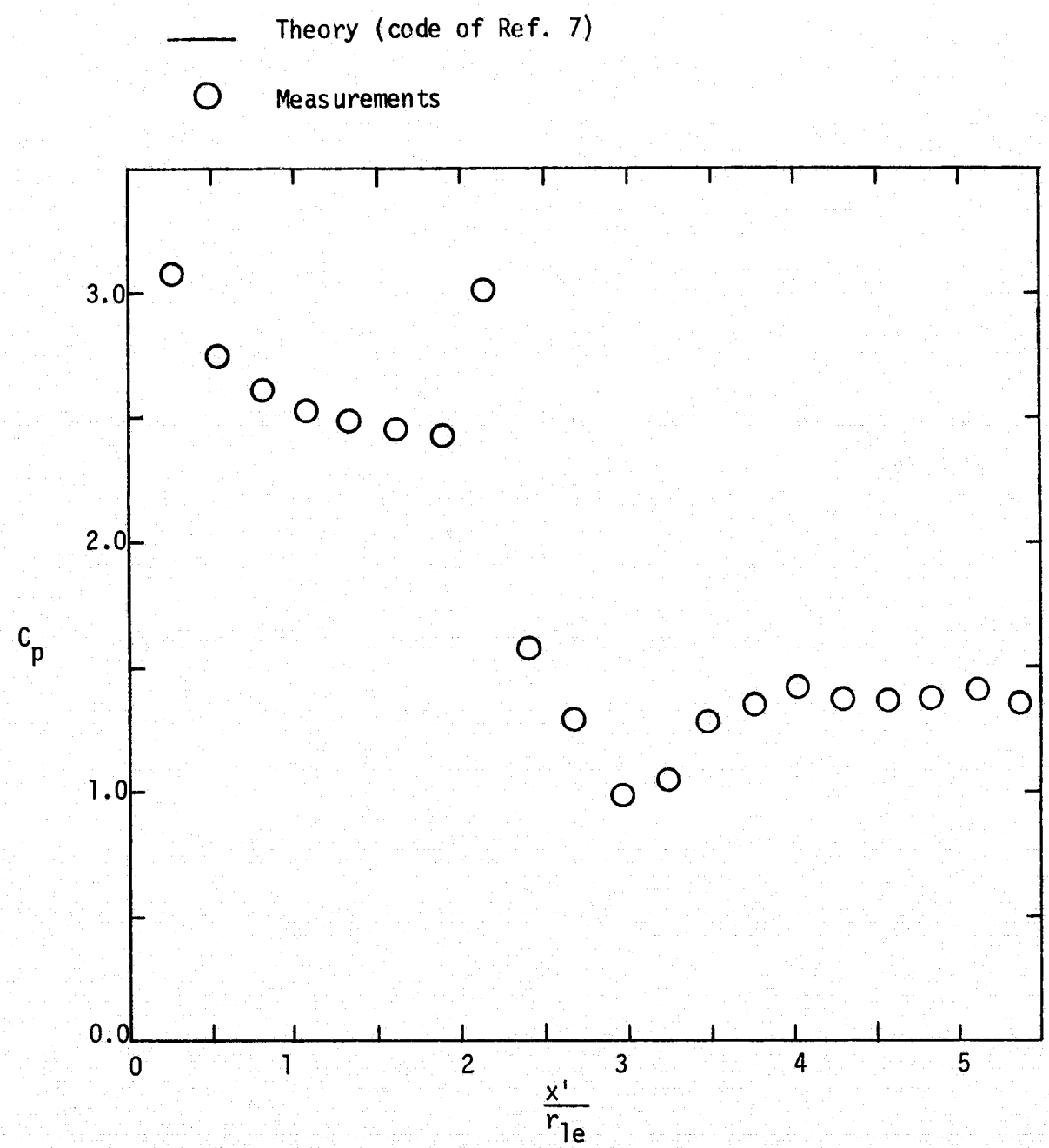

(a) $\Lambda = 30°$ (SC 17)

Figure 8. - The experimentally-determined pressure coefficient distributions as compared with the theoretical distributions in the plane of symmetry.

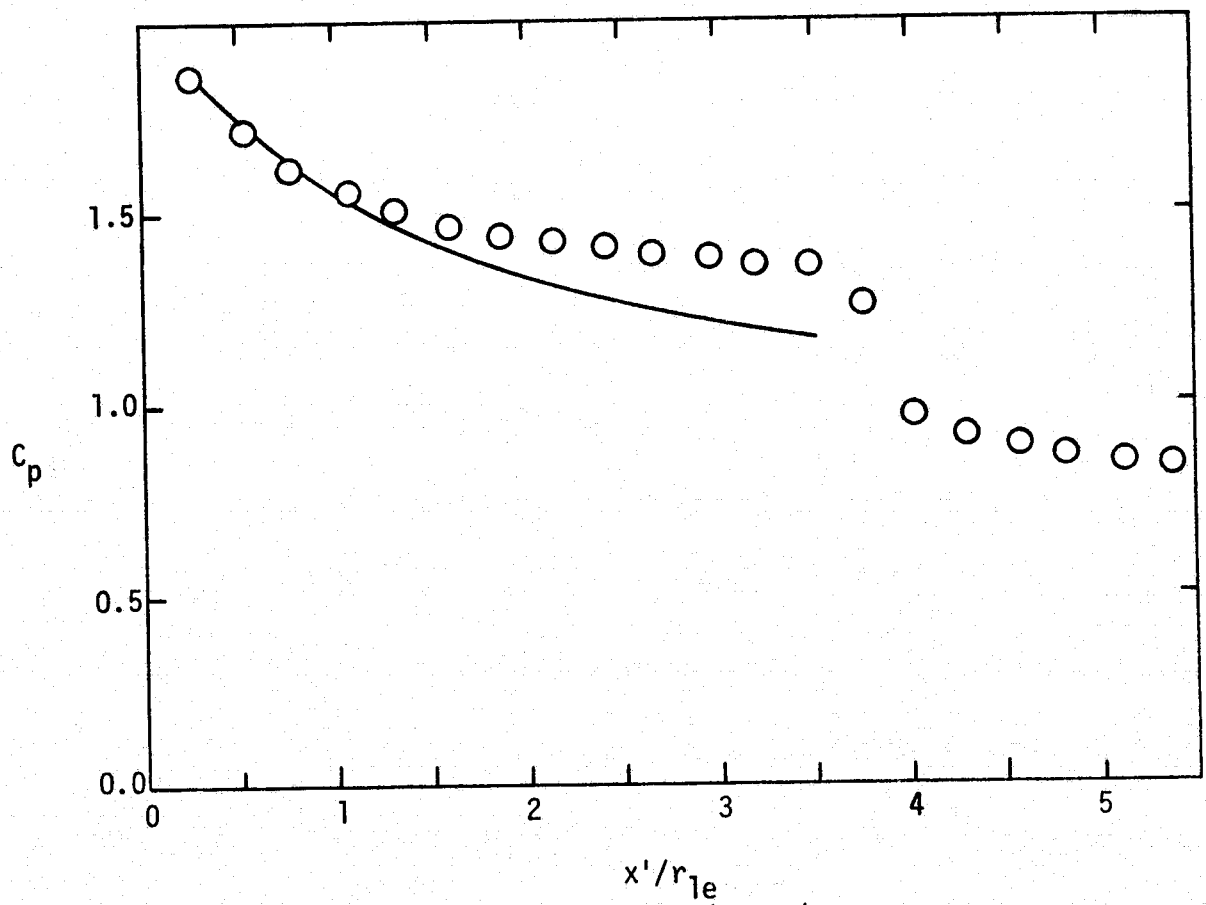

(b) Λ = 45° (SC 20)

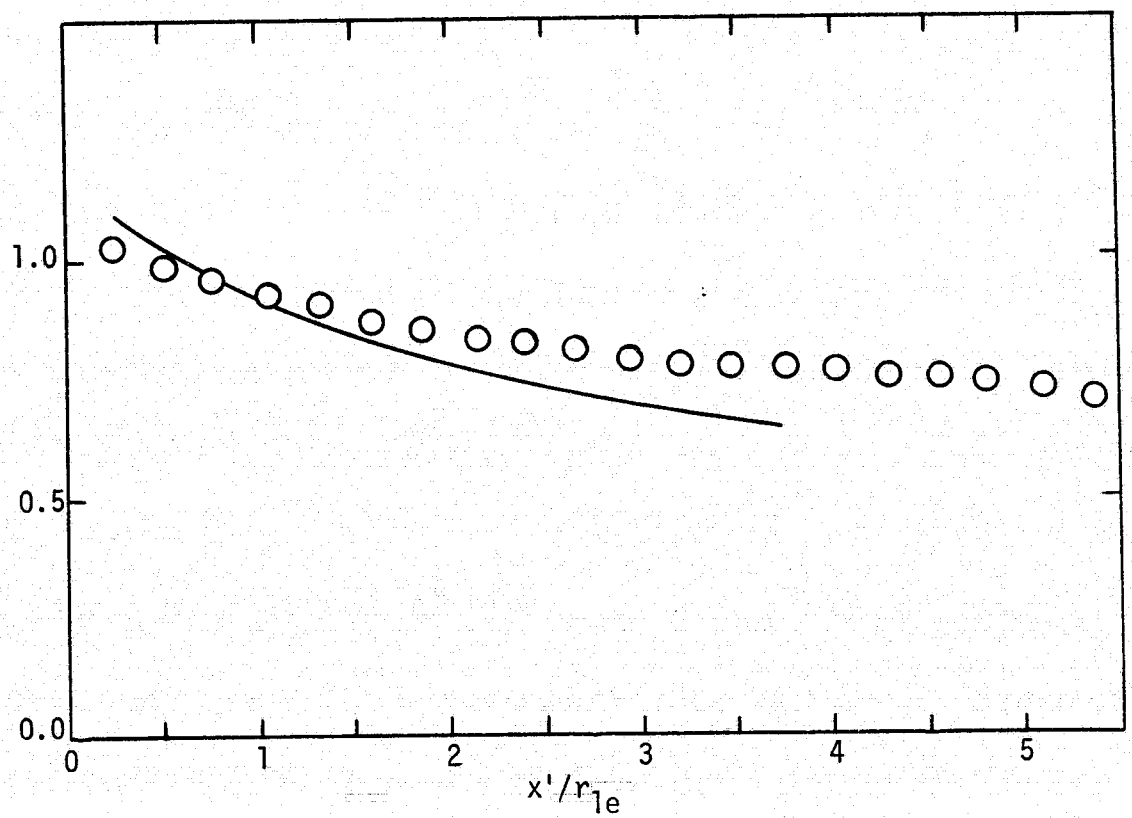

(c) Λ = 55° (SC 23)

Figure 8. - Continued.

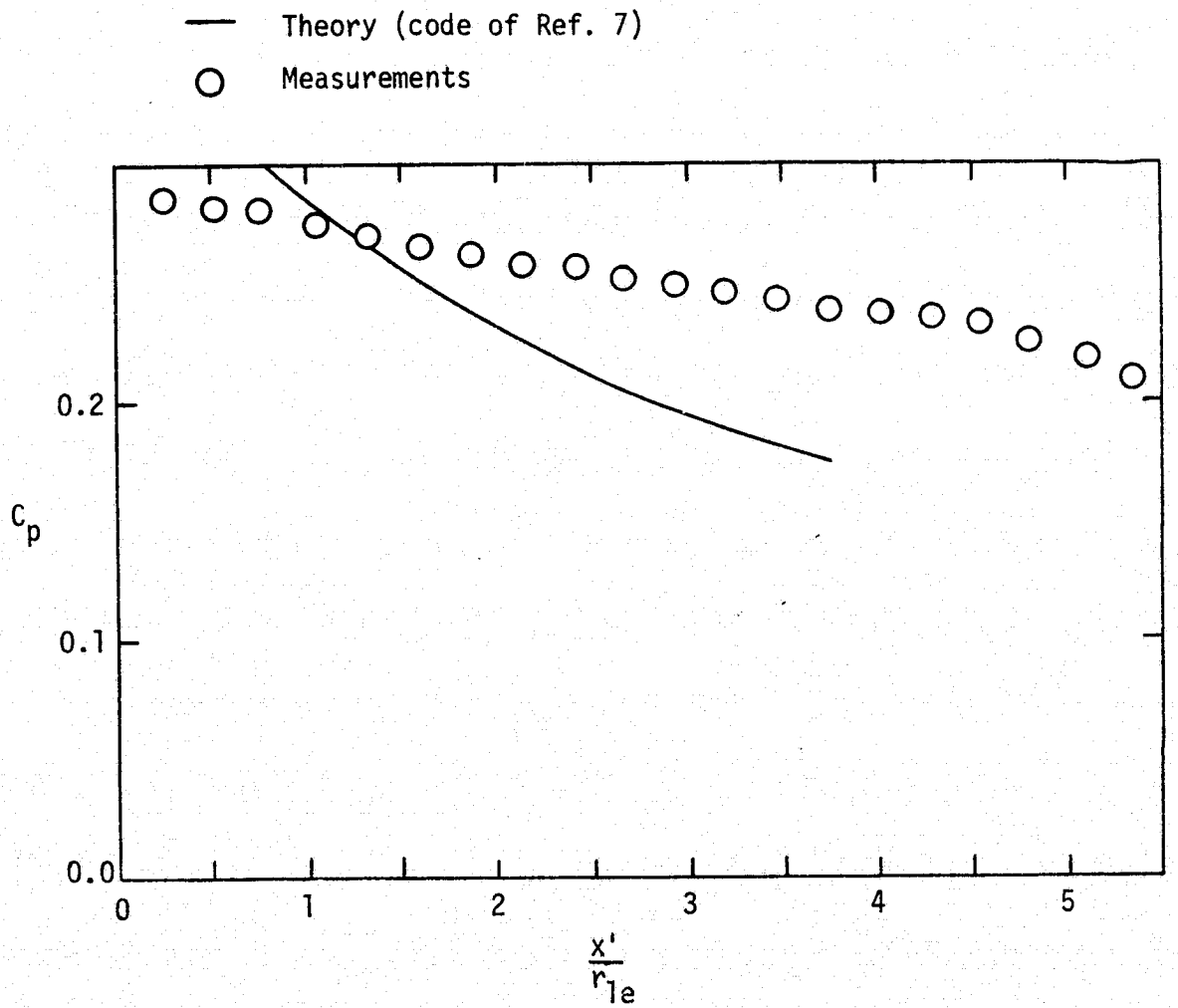

(d) $\Lambda = 70°$ (SC 26)

Figure 8. - Continued.

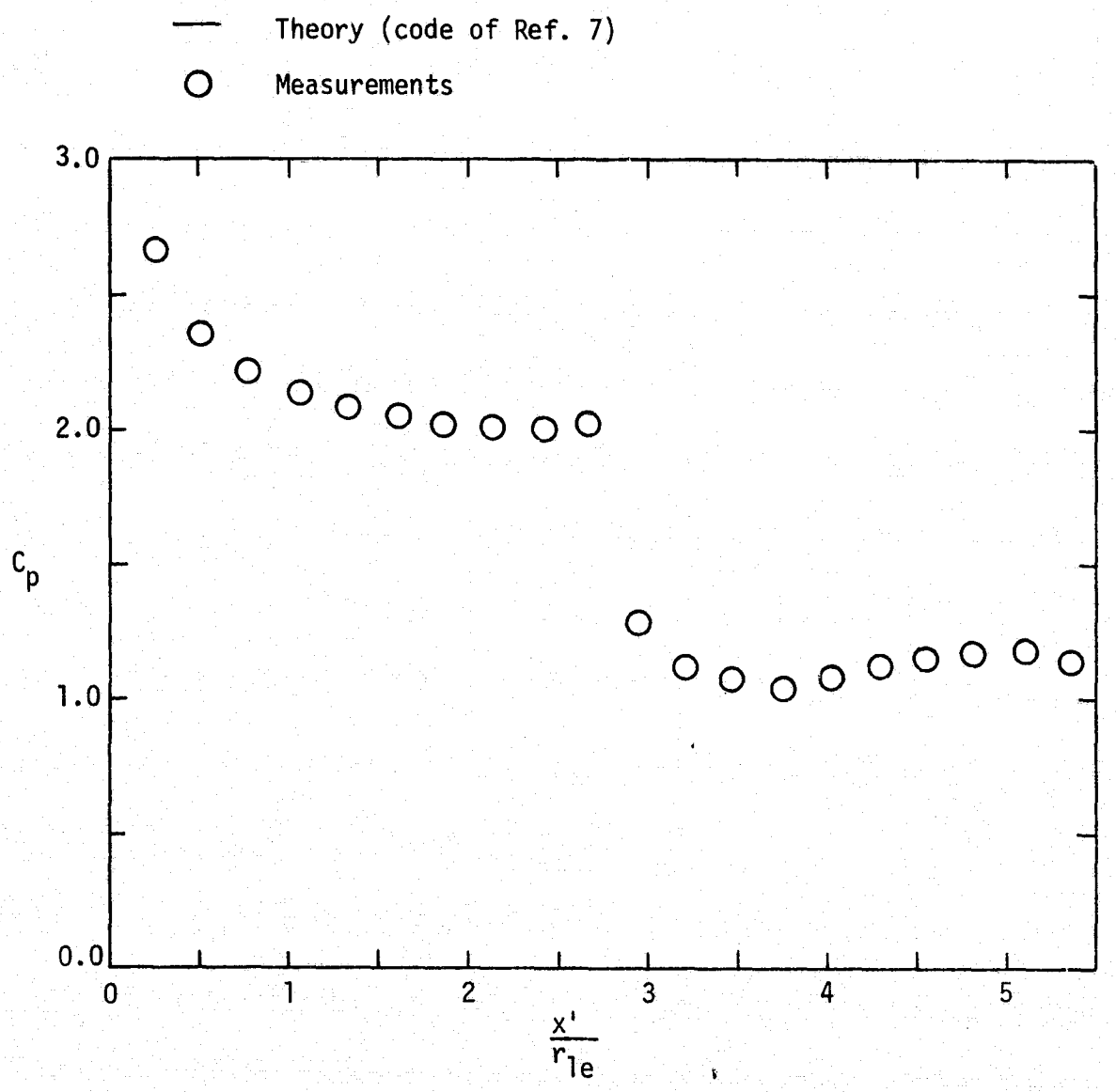

(e) $\Lambda = 36°$ (SC 37)

Figure 8. - Continued.

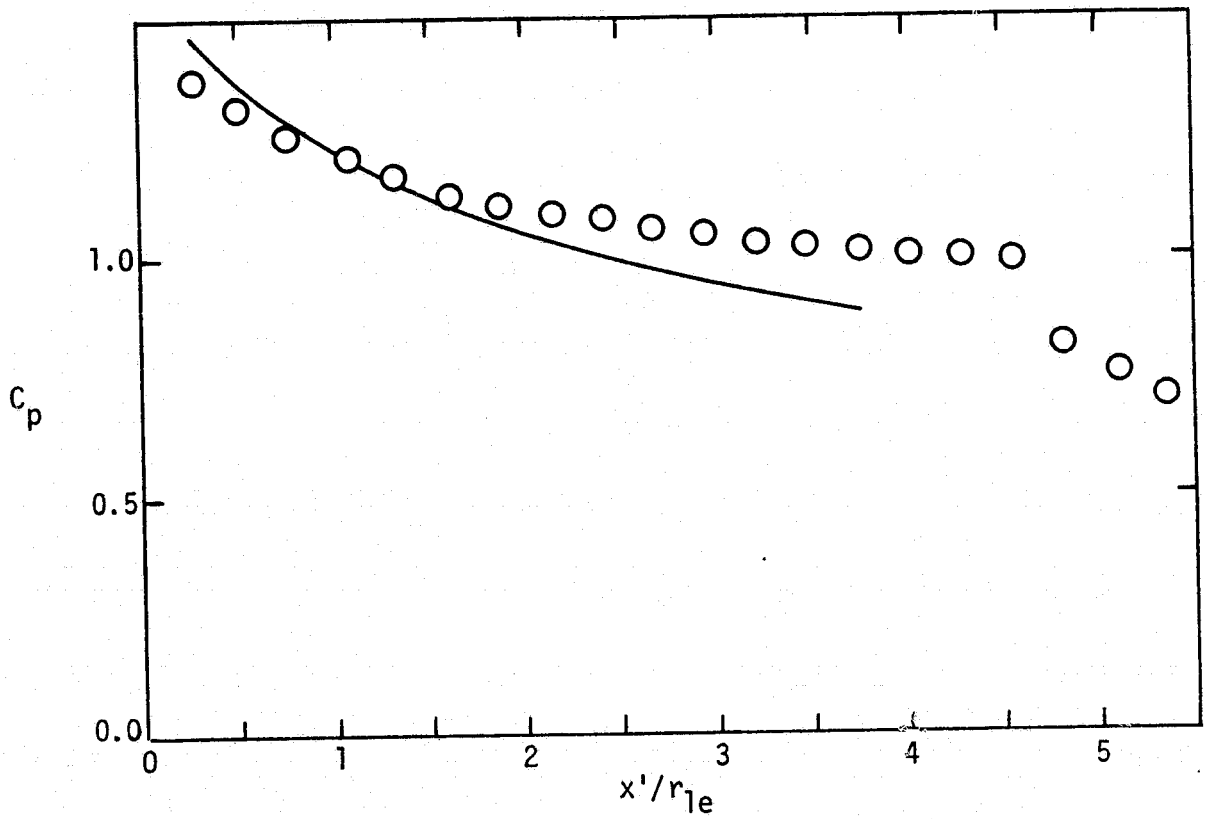

(f) $\Lambda = 50°$ (SC 22)

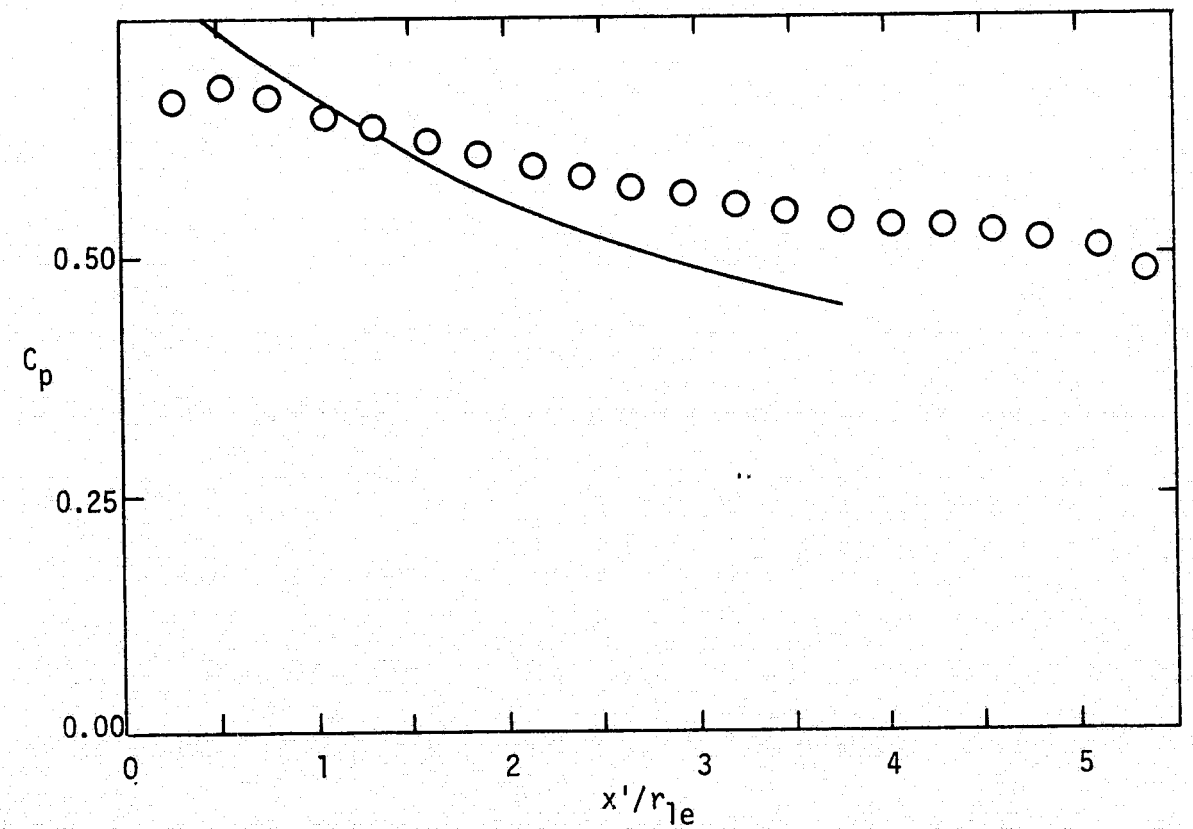

(g) $\Lambda = 60°$ (SC 24)

Figure 8. - Concluded.

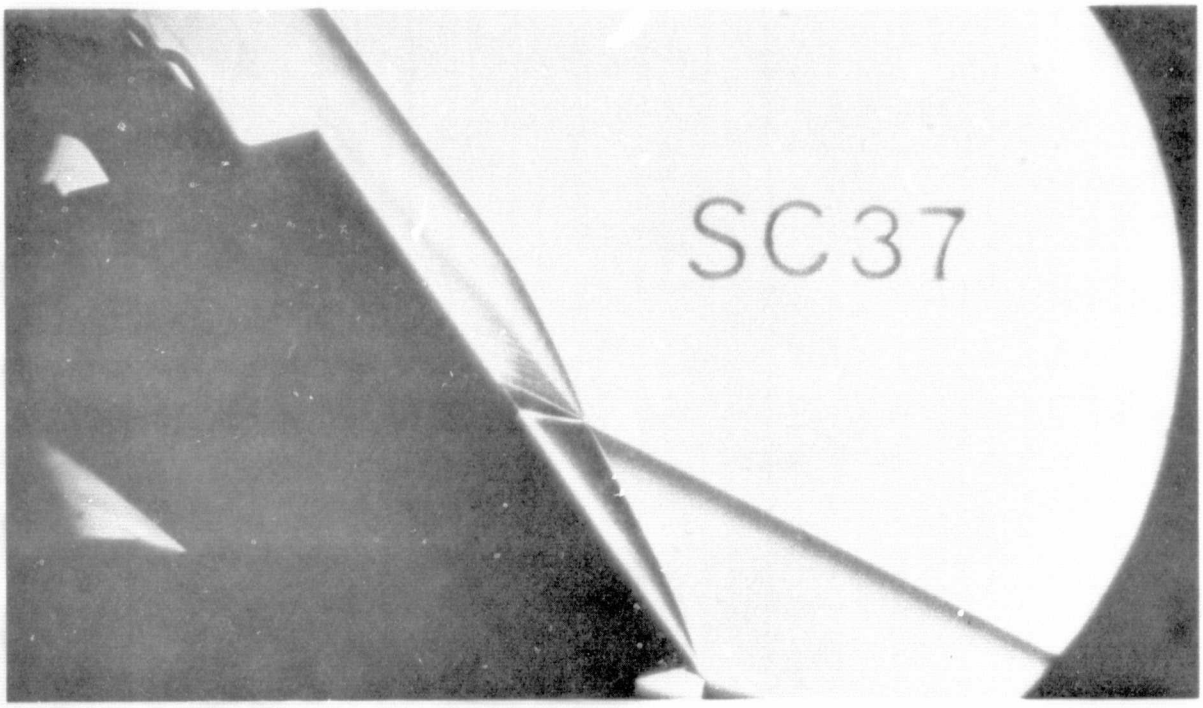

(a) Λ = 36° (SC 37)

(b) Λ = 50° (SC 22)

Figure 9. - Additional schlieren photographs.

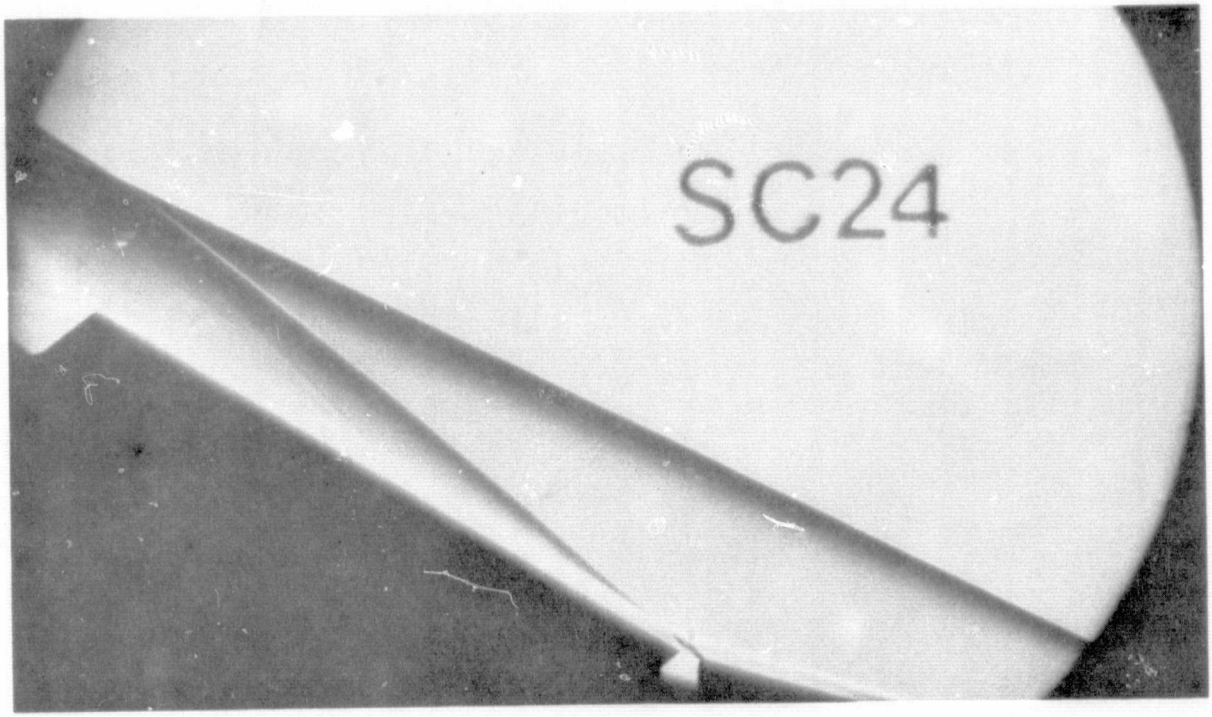

(c) $\Lambda = 60°$ (SC 24)

Figure 9. - Concluded.

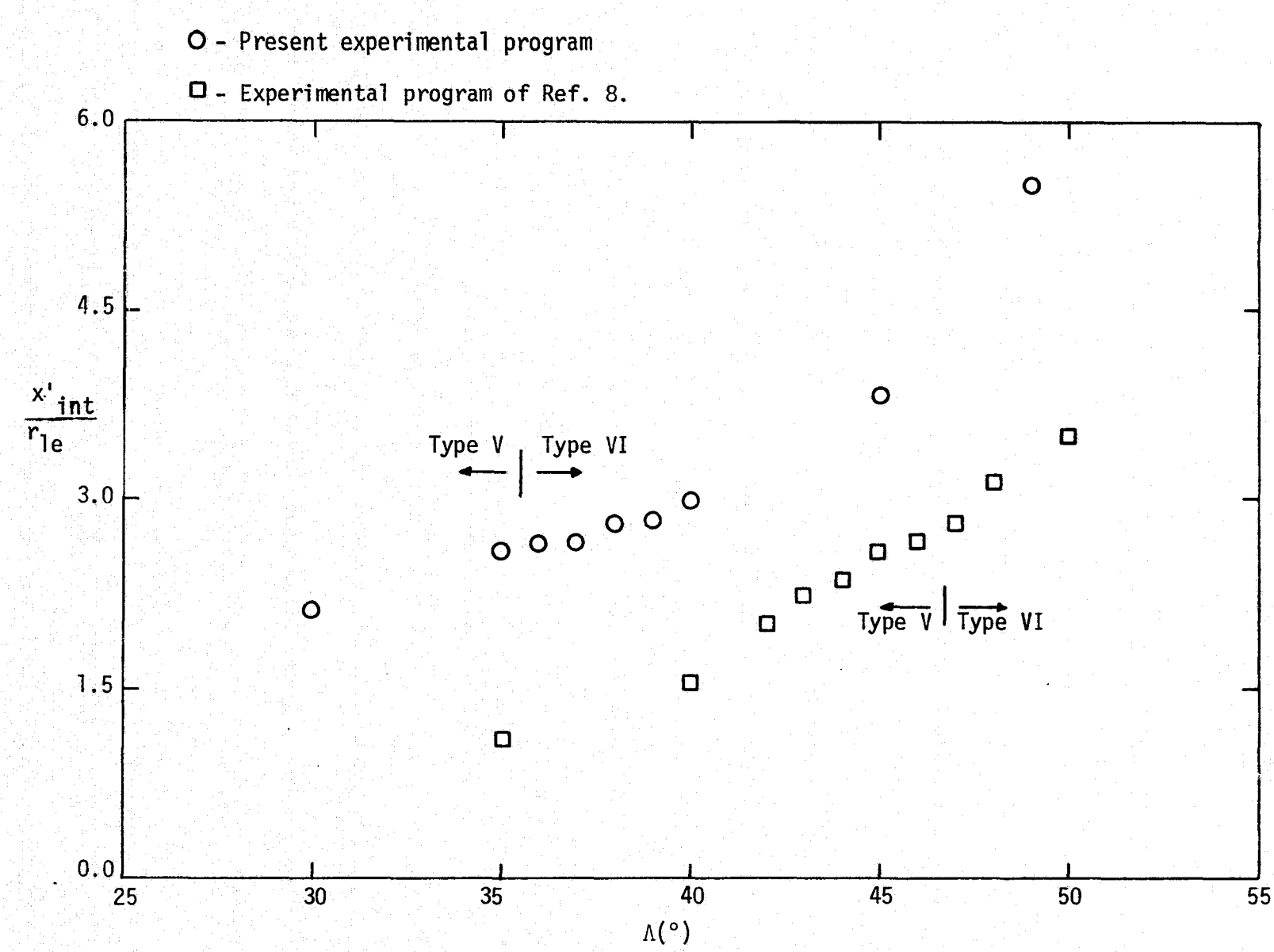

Figure 10. - Comparison of the location of the interaction-perturbed impingement region as a function of sweep angle for the present wedge-cylinder configuration and the double-wedge configuration of Ref. 8.

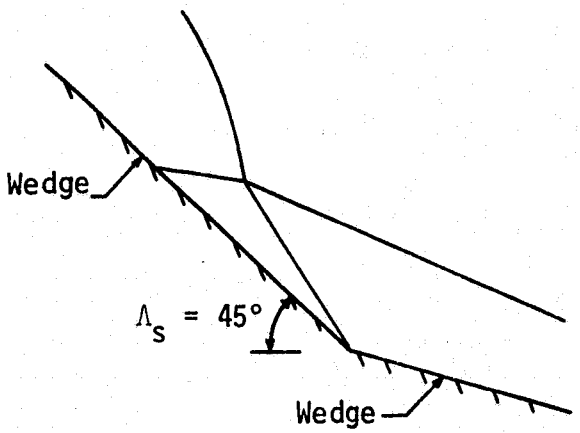

(a) Double-wedge configuration

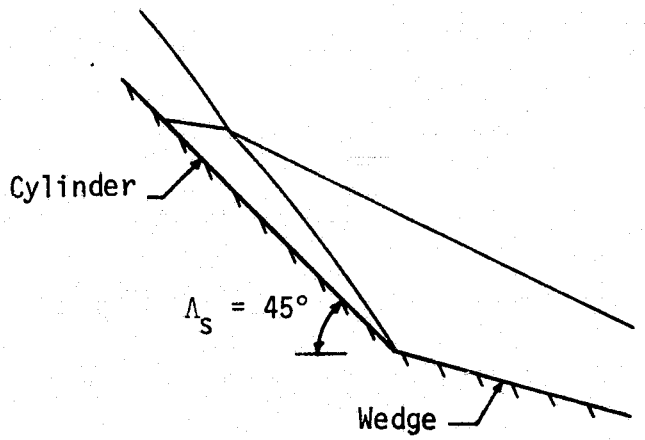

(b) Wedge-cylinder configuration

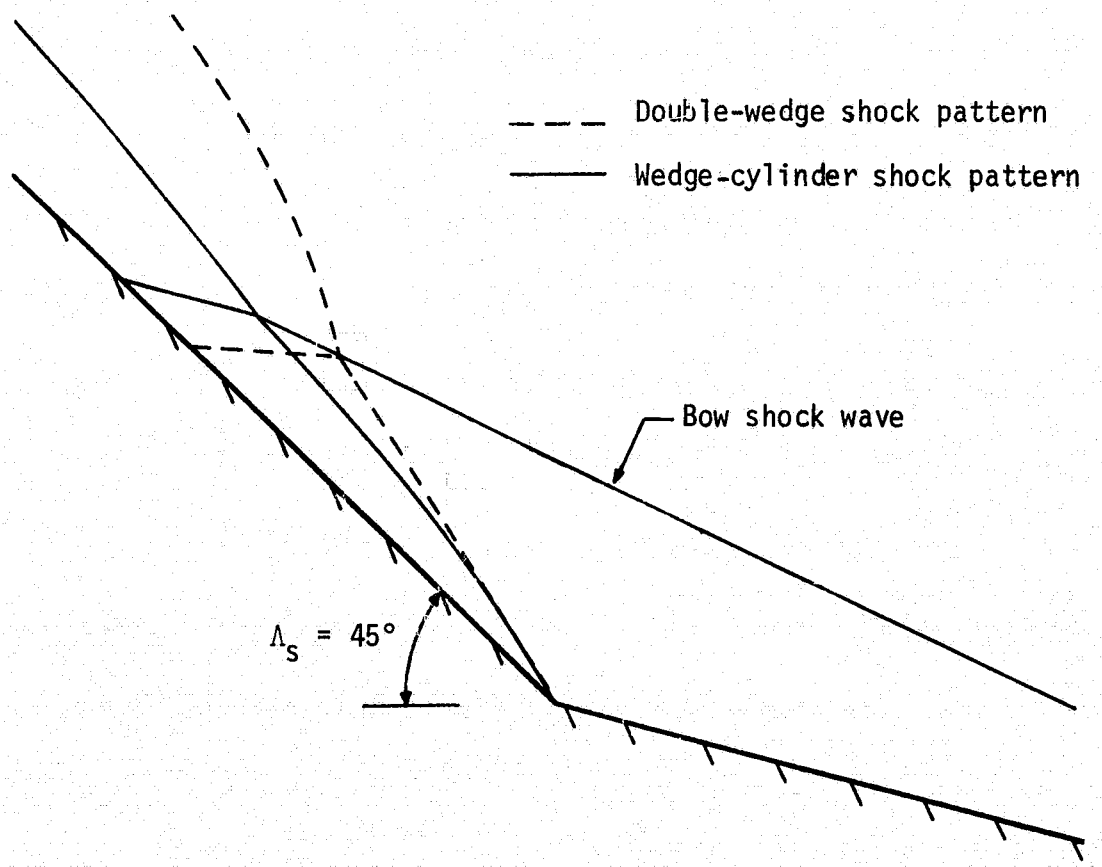

(c) Superposition of shock patterns.

Figure 11. - Comparison of impingement regions resulting from shock-shock interactions for the present wedge-cylinder configuration and the double-wedge configuration of Ref. 8.

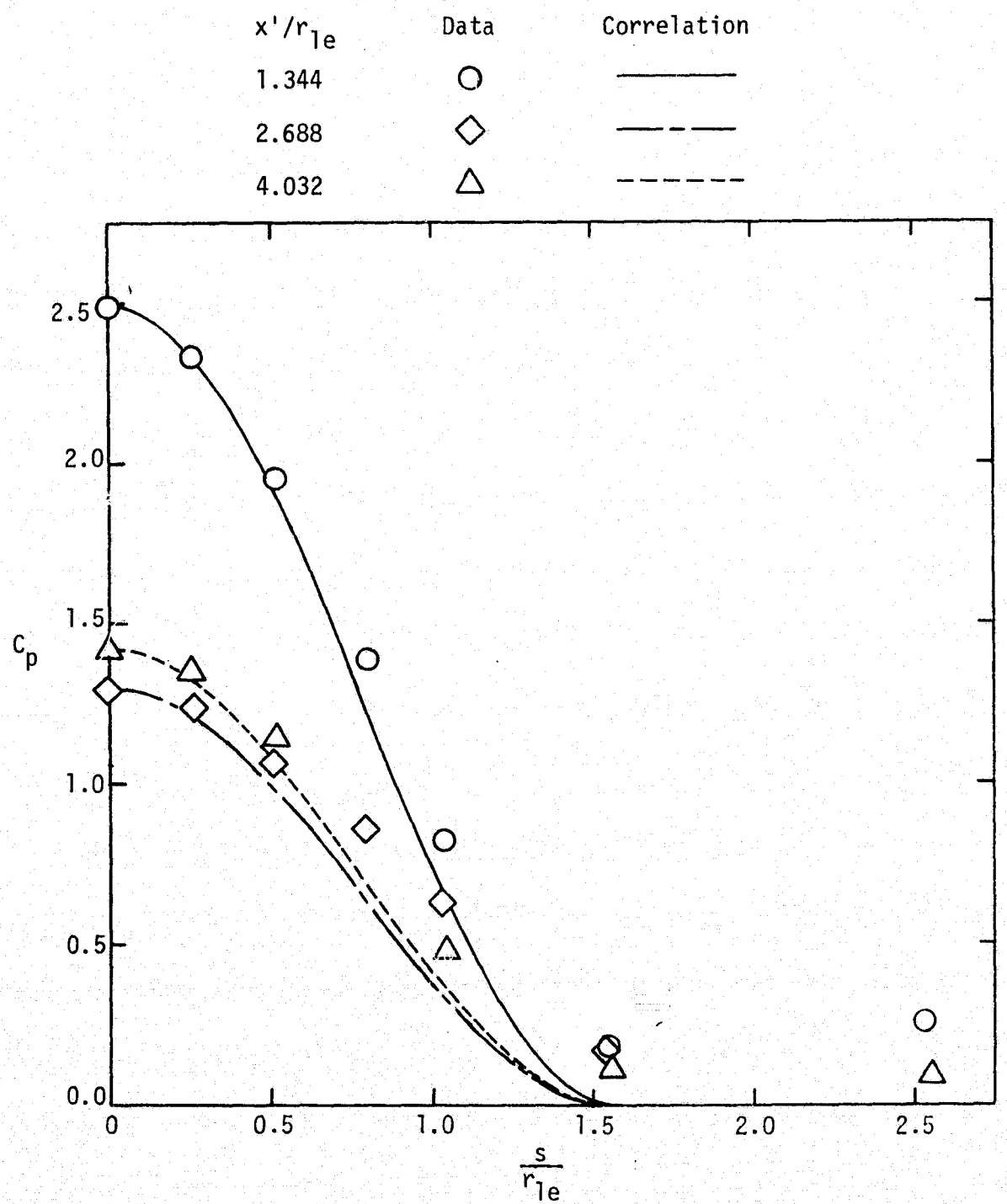

(a) $\Lambda = 30°$ (SC 17)

Figure 12. - Experimentally-determined crossflow pressure coefficient distribution compared with theoretical distribution using modified Newtonian flow.

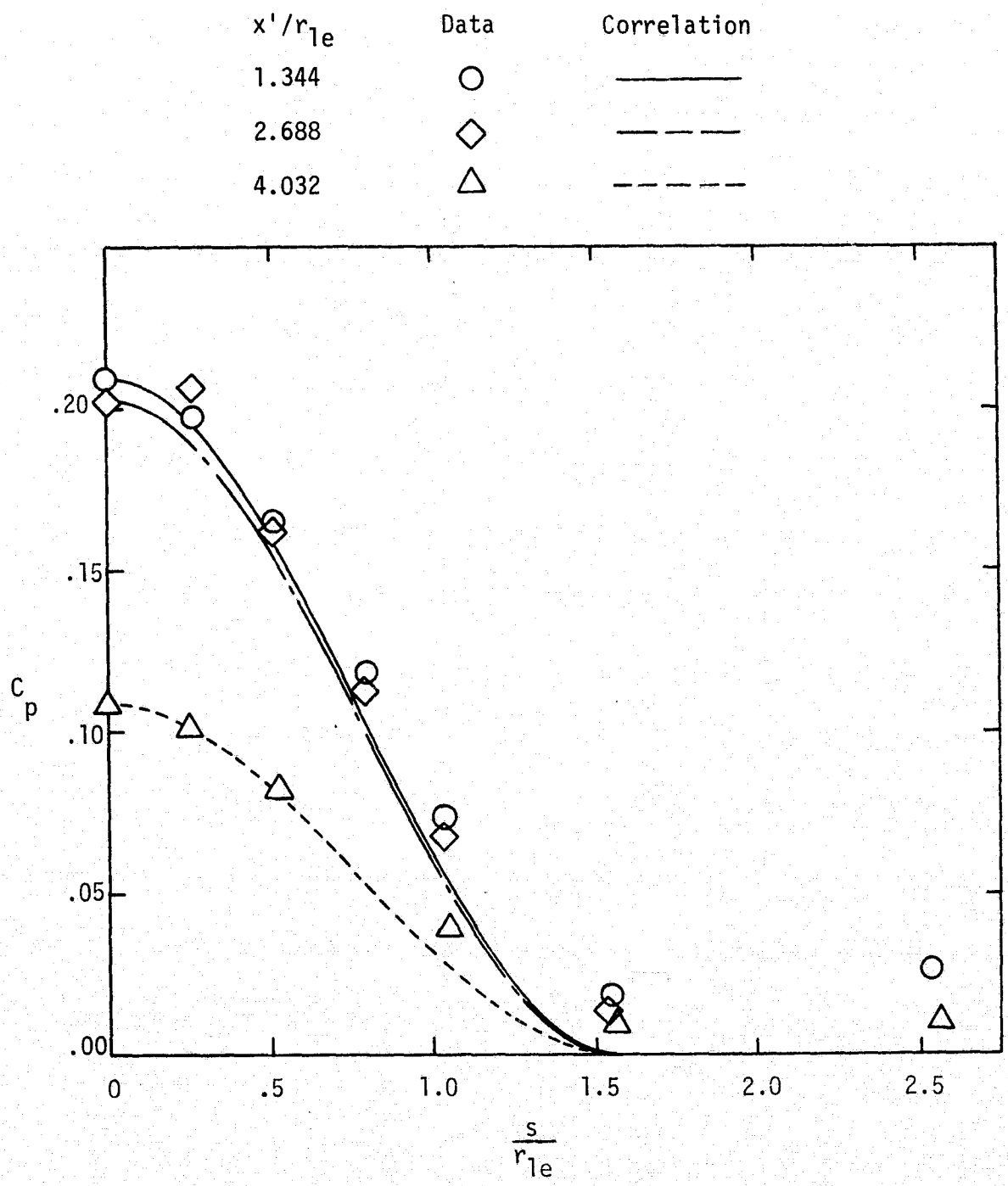

(b) $\Lambda = 36°$ (SC 37)

Figure 12. - Continued.

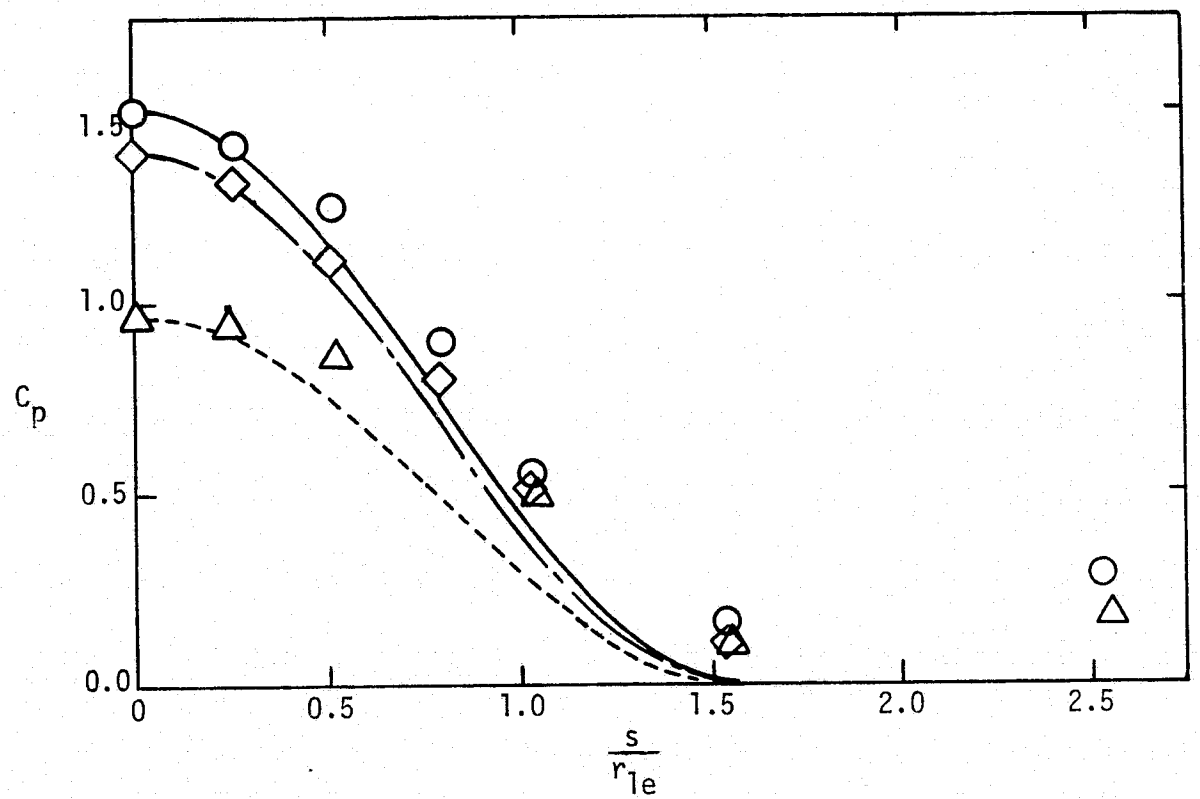

(c) Λ = 45° (SC 20)

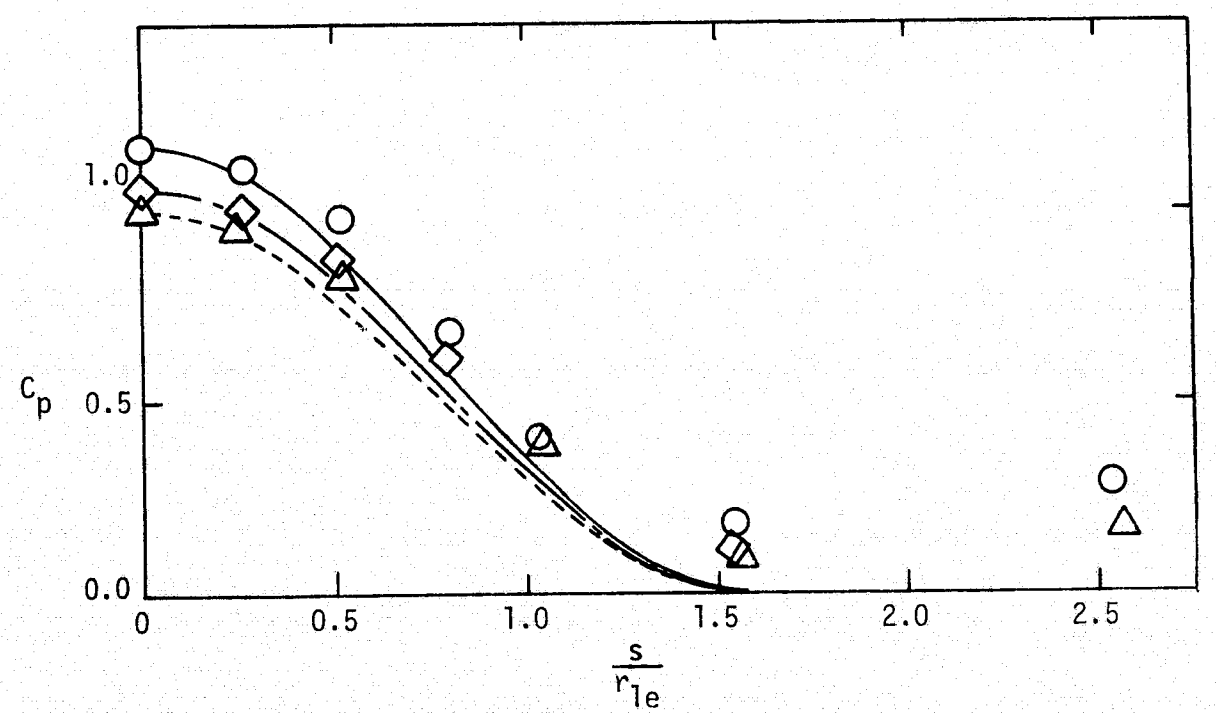

(d) Λ = 50° (SC 22)

Figure 12. - Continued.

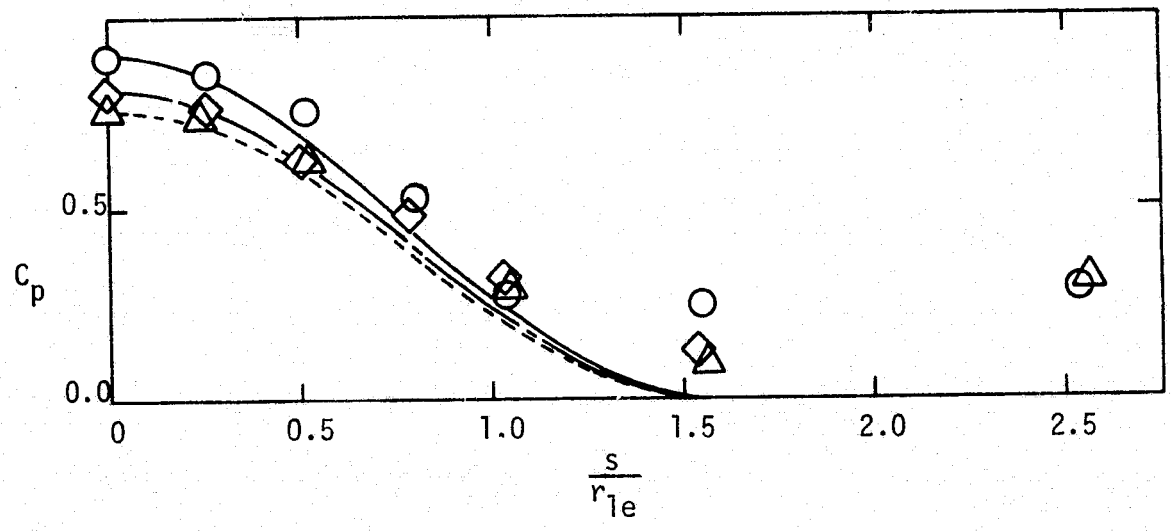

(e) $\Lambda = 55°$ (SC 23)

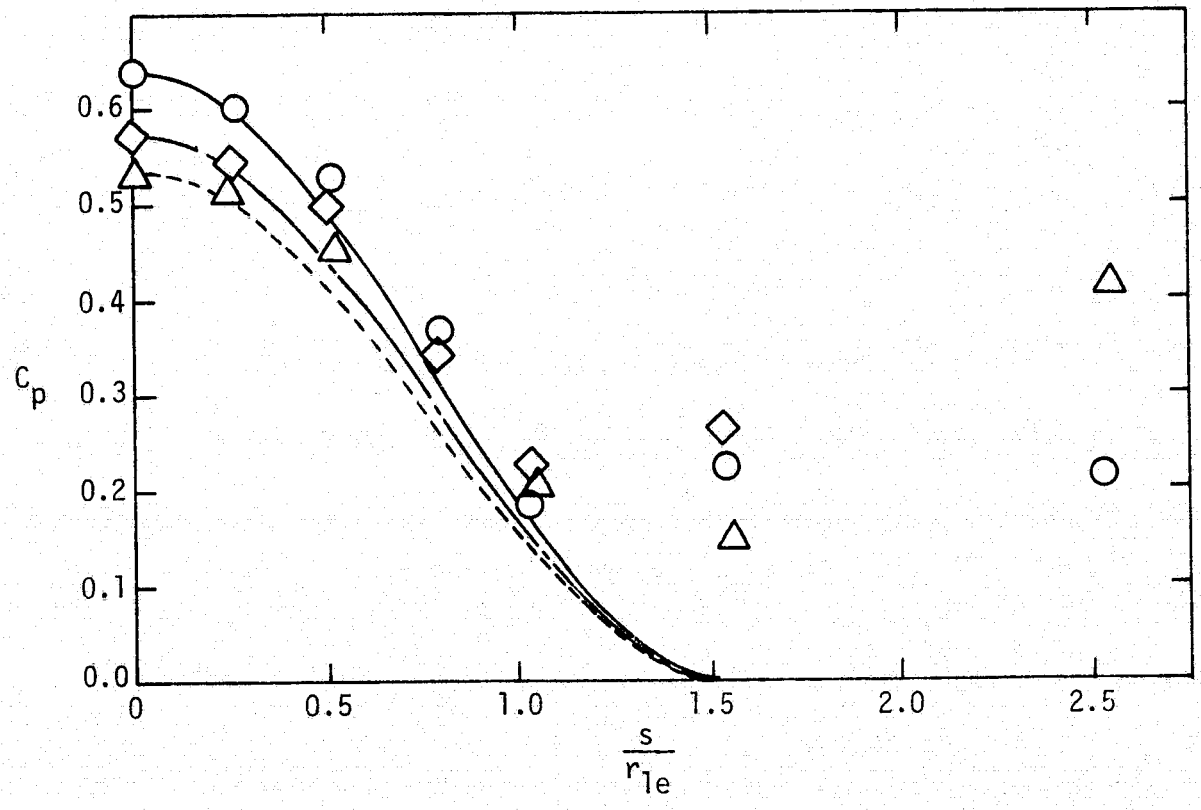

(f) $\Lambda = 60°$ (SC 24)

Figure 12. - Continued.

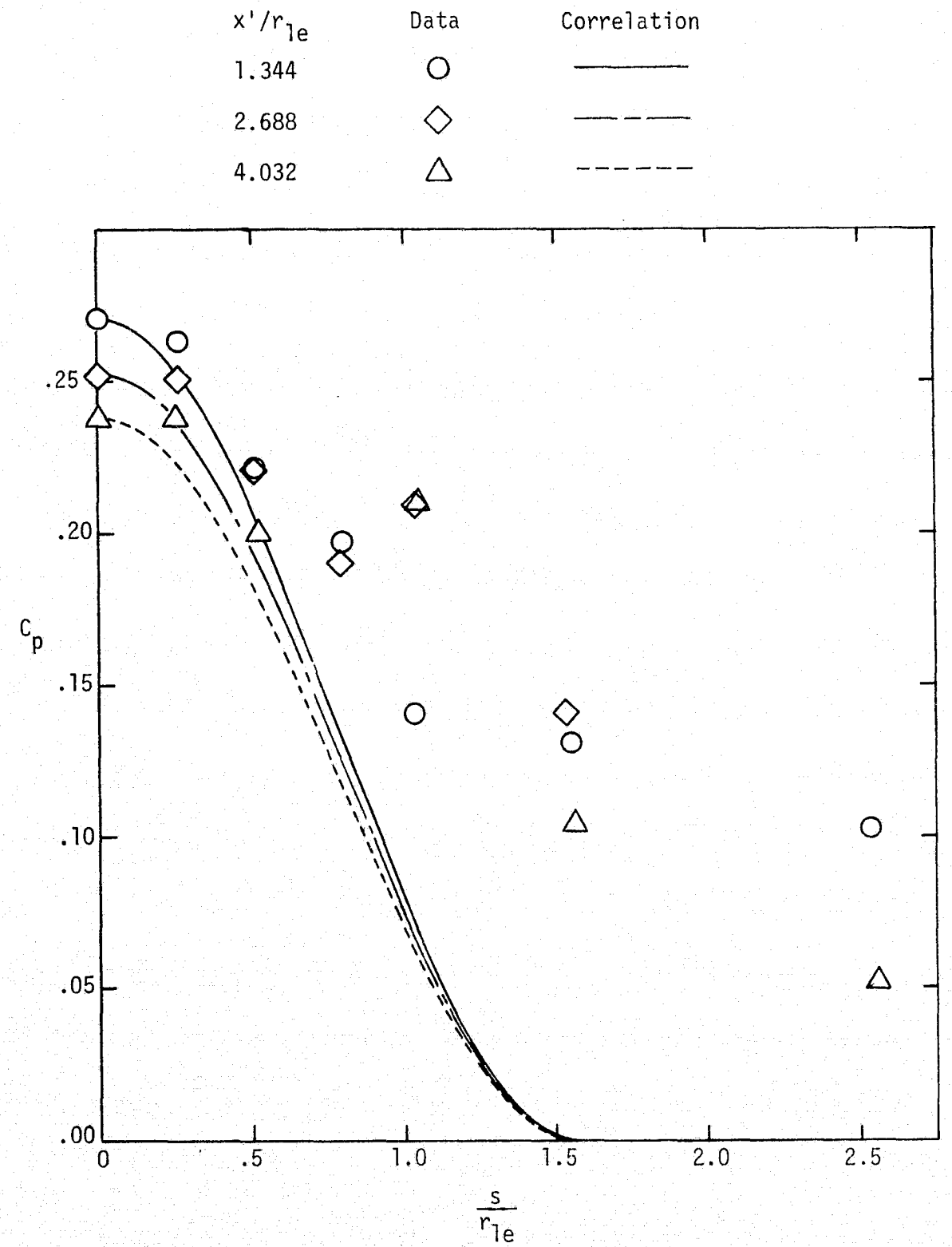

(g) $\Lambda = 70°$ (SC 26).

Figure 12. - Concluded.